7-2011

MONITORING OF MESENCHYMAL BASED CONSTRUCTS USING MAGNETIC RESONANCE ELASTOGRAPHY

Evan T. Curtis
University of Nebraska-Lincoln, ecurtis@huskers.unl.edu

MONITORING OF MESENCHYMAL BASED CONSTRUCTS USING MAGNETIC RESONANCE ELASTOGRAPHY

by

Evan T. Curtis

A THESIS

Presented to the Faculty of
The Graduate College of the University of Nebraska
In Partial Fulfillment of Requirements
For the Degree of Master of Science

Major: Agricultural and Biological Systems Engineering

Under the Supervision of Professor Shadi F. Othman

Lincoln, Nebraska
July, 2011

MONITORING OF MESENCHYMAL BASED CONSTRUCTS USING MAGNETIC RESONANCE ELASTOGRAPHY

Evan T. Curtis, M.S.

University of Nebraska, 2011

Advisor: Shadi F. Othman

Evaluating the functionality of an engineered material lies in the proper characterization of its material and functional properties. In the treatment of musculoskeletal disorders, engineered bone or fat tissue must behave as an adequate replacement else failure of the material could result in discomfort and further surgical procedures. A significant material characteristic that reflects tissue development is the mechanical properties (i.e. shear strength and viscosity). Shear strength and viscosity provide an indication of how efficient the material is in dissipating energy. Energy dissipation occurs naturally in many tissues including fat and can prevent damage to deeper tissues. Many of the techniques for determining a material's shear modulus result in the destruction of the construct. However, few methods exist that can assess this property by evaluating a noninvasive cross-section of the construct. As a result a need exists for the development of a nondestructive way to assess the biomechanical properties of engineered materials both before and after they have been implanted. In an effort to improve the quality of constructs being produced, a recently developed magnetic resonance imaging (MRI) technique termed magnetic resonance elastography (MRE) was applied to evaluate the development of adipogenic (fat) and osteogenic (bone) tissue constructs derived from mesenchymal stem cells. MRE is a technique in which motion from a mechanical actuator is synchronized to a phase contrast imaging pulse sequence

and used to measure the generated displacement. The captured displacement is displayed in shear wave images from which the properties of shear stiffness can be derived. For differentiation of the bone marrow-derived mesenchymal stems cells, the use of differentiation media kits was applied. Change in stiffness was observed over the four weeks of *in vitro* growth. Constructs initially measured at approximately 3 kPa developed into 22 kPa osteogenic and 1 kPa adipogenic tissues. Following four weeks *in vitro* growth, constructs were implanted in athymic mice and assessed with an MRE system custom built for animal imaging. The following thesis demonstrates the application of MRE to evaluate the mechanical properties of engineered constructs through *in vitro* growth and *in vivo* regeneration in an animal model.

TABLE OF CONTENTS

LIST OF FIGURES AND TABLES

CHAPTER 1: BACKGROUND AND GOALS

Motivation

Patients suffering from burn injuries, cancer resections, bone and cartilage loss, or degenerative disease are in need of a viable and cost effective solution. In 2010, 18.4 million soft tissue surgeries were performed with four million cases being related to tumor removal (American Society of Plastic Surgeons, 2011). Overall, the total expense of the 18 million procedures was approximately $10.1 billion. In addition to the financial burden, soft tissue defects as well as resections from breast and facial cancer leave patients with disfiguration and traumatic challenges (Patrick, 2001). Beyond soft tissue procedures, approximately 500,000 bone graft operations are conducted annually in the United States, resulting in approximately $1.5 billion in sales of bone graft and bone graft substitutes (Greenwald et al., 2001).

The main solution for many of the above needs is the use of transplantable tissue either retrieved from other locations on the patient or another person. However, availability of transplantable tissue is not always reliable and to complicate matters direct tissue grafts can suffer from donor site morbidity that can lead to further procedures, trauma and medical expenses (Rozen et al., 2009; Patrick C. W., 2001). A potential alternative to direct transplantation of tissues is the use of tissue engineering (TE) to develop more robust constructs to treat regions of dead or diseased tissue. The development of engineered tissues requires careful attention to the material's properties. For example, the mechanical properties are a relevant indicator of tissue growth and functionality. To improve the quality of available engineered constructs, a need exists to develop methods to better characterize their mechanical properties (Mauck et al., 2000;

Kotlarchyk et al., 2010). Proper characterization will assure that the material will behave correctly in the transplanted environment and not cause further complications. The following thesis outlines the development and potential use of Magnetic Resonance Elastography (MRE) as a means to monitor the development of engineered constructs.

Key Concepts

- **Tissue Engineering and Mesenchymal Stem Cells**

A goal of TE is to create functional biological replacements for various tissues of the human body (Butler et al., 2000). To accomplish this goal, it is necessary to rely on the principles of biology, cell transplantation, material science, and engineering to combine the appropriate cells, growth factors, and biomaterial scaffolds to create a functional tissue. Cells that can potentially be used in TE range from somatic differentiated cells to embryonic stem cells or adult stem cells, which can potentially be differentiated with the proper factors to many tissue lineages (Caplan et al., 1994; Langer and Vacanti, 1993; Magli et al., 2000). Bioactive signals may be used to direct tissue regeneration, remodeling, or cell differentiation using chemical factors or physical excitation (electrical, mechanical, or surface-induced) (Heng et al., 2004; Altman et al., 2001; McBeath et al., 2004). In the case of stem cells, after differentiation, the mixture of cells and reagents can be left to expand *in vitro* for a specified period before being seeded onto a scaffold or can be directly seeded onto the scaffold (Alhadlaq et al., 2004). The scaffold serves as a physical support to localize and maintain cells and should provide an environment in which appropriate regulation of cellular behavior (adhesion, proliferation, migration, and differentiation) can occur such that a functional tissue can form.

Biomaterial scaffolds can be produced from natural (e.g., collagen) or synthetic (e.g., polyethylene glycol) materials (Glowacki et al., 2008; Tsang and Bhatia, 2004).

For any material or tissue engineered construct that is being designed for potential human implantation, it has been, and continues to be, essential that the engineered materials exhibit the necessary mechanical properties (i.e. hardness, elasticity, yield strength) to achieve and maintain functionality (Butler et al., 2000). Understanding of material performance is critical since during TE construct growth, mechanical properties change due to cellular responses and material remodeling, including stem cell differentiation, cellular contraction, scaffold remodeling, and biodegradation of the scaffold (Dado and Levenberg, 2009; Choi et al., 2010). For example, in bone engineering a cell-seeded biomaterial scaffold has to serve as a support to the cells, as well as mechanical support to the injury site, gradually transferring the load as the scaffolds degrades to accommodate the regenerating tissue (Yaszemski et al., 1996; Leong et al.. 2003; Mistry and Mikos, 2005). However, the engineered bone or adipose tissue must behave as an adequate replacement else failure of the material could result in discomfort and further surgical procedures.

For bone tissue engineering, mesenchymal stem cells (MSCs) isolated from bone marrow were identified to have a strong capability for inducing the osteogenic phenotype (Friedenstein, 1976). Bone marrow is naturally the source of osteoblasts and osteocytes. Osteoblasts are essential for synthesis and regulation of bone extracellular matrix deposition and mineralization while osteocytes are the supporters for bone matrix calcification. Beyond bone development, a major property of MSCs is their ability to be induced into multiple cell lineages such as fat and cartilage (Pittenger et al., 1999). Such

discovery has enabled MSCs to be investigated as an alternative for soft tissue reconstruction (Alhadlaq and Mao, 2004). As researchers continue to study the behavior and medicinal utility of MSCs *in vitro*, investigation has been extended into the use of animal models and clinical trials (Patrick et al., 2008; Derubeis and Cancedda, 2004).

- **Characterization Methods**

Characterization methods are one of many gate keepers applied in regulating the translation of products from the lab bench to the clinical setting. Characterization of engineered materials is accomplished with a variety of tools, many of which compromise the usefulness of the sample after testing. In culture, tissue engineers evaluate cell morphology and activity through the use of microscopy, biochemical assays and histologic stains. While such histologic procedures provide a representation of molecular content and signaling pathways – for example, staining for alkaline phosphatase (ALP) serves as an early osteogenic marker – it is destructive to the tissue (Sabokbar et al., 1994). As a noninvasive means of assessment, imaging methods such as micro-computed tomography (micro-CT), ultrasound (US), and magnetic resonance imaging (MRI) have been applied (Jones et. al., 2009; Kim et al., 2008; Peptan et al., 2006).

To date, the use of imaging technologies has contributed modestly to understanding of regenerating tissue. Many imaging modalities have attempted to be used, but possess limitations, noted in parentheses, in assessing engineered tissues including optical and fluorescent microscopy (low penetration depth), US (low resolution), and micro-CT (use of ionizing radiation) (Helmchen and Denk, 2005; Jones et. al, 2009; Kim et al., 2008). However, MRI has been demonstrated to potentially play an important role in tissue engineering through different contrast mechanisms including

T_1, T_2, diffusion, and magnetization transfer (MT). MR contrast is achieved through studying spin (proton) behavior under a strong magnetic field coupled with radio frequency (RF) and magnetic field gradients for spin manipulation and spatial localization, to acquire quantitative images to describe flow, molecular content, and MR physical properties (Xu et. al, 2008; Haacke et al., 1999; Bernstein et al., 2004). MRI-based techniques were identified by several research groups as a novel tool for assessing the structure and composition of TE bone constructs (Washburn et al., 2004; Xu et al., 2006; Hartman et al., 2002; Potter et al., 2006). These studies correlated different measured MR parameters (e.g., T2 relaxation time, shear stiffness, and MT ratio) with mineral deposition and molecular content. In addition to determining morphologic information, some of these methods have developed the ability to assess mechanical properties. One technique for the measurement of mechanical stiffness via MRI is through a technique termed MRE.

- **MRE Basics**

MRE introduces a new quantitative parameter where measurement of cyclic shear wave motion in biological tissues provides unique spatially-localized information about the tissue's material properties (Muthupillai et al., 1995; Muthupillai et al. 1996). MRE was originally developed to enhance disease diagnosis by allowing organ stiffness palpation through the visualization of induced low frequency spin motion. Since its first implementation, MRE has been applied clinically for the assessment of organ pathology. MRE has been implemented for detecting breast cancer (McKnight et al., 2002), as well as for the visualization of the elastic properties of the brain (Wuerfel et al., 2010; Clayton et al., 2011), and even bovine articular cartilage degradation with improved

instrumentation (Lopez et al., 2008). With increased availability of higher field magnets, MRE has been extended to the microscopic scale where high resolution MRE to monitor tissue engineered constructs regeneration has been demonstrated (Othman et al., 2005; Othman et al. 2011).

Operation of MRE requires three essential components: a motion source, a pulse sequence, and an inversion algorithm. The motion component, often an acoustic actuator, is coupled to the tissue of interest to induce shear wave motion. Second, a pulse sequence using bipolar gradients (motion-sensitizing gradients ─ MSG), synchronized with the acoustic shear waves, is used to encode the motion as MR phase difference images. The sequence provides the acquisition timing to generate images that effectively represent quantitative snapshots of tissue displacement caused by propagating mechanical waves. Finally, an inversion algorithm uses the measured displacements to calculate the shear stiffness distribution in the tissue (Muthupillai at al., 1995). Figure 1 illustrates a typical MRE setup.

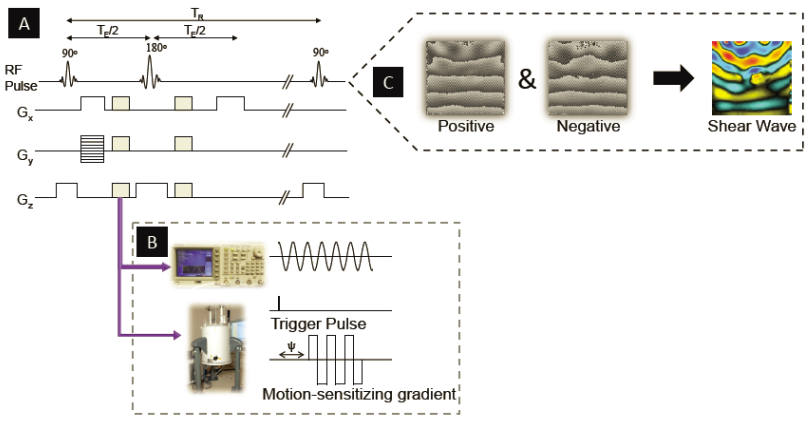

Figure 1. The acquisition process for regenerative elastography. A pulse sequence (a) controls the synchronization (b) of the function generator with the bipolar gradient pulses of the MRI scanner. Following the acquisition of bipolar gradients toggled in positive and negative orientations, (c) a shear wave image is produced using complex division.

MRE, similar to MRI, is a phase sensitive technique where after the Fourier transform of the raw data, the magnitude and phase values are retrieved in each pixel; and the phase of a signal only has a meaning when the signal is repetitive or cyclic (Moran et al., 1985). Usually when the magnitude image is presented, phase information is superimposed within the magnitude information. By accessing the phase information of the complex reconstructed image $\hat{p}(x,y)$ alone, additional encoded information can be discovered and applied to detect, for example, magnetic field homogeneity, MR temperature mapping as well as MRE (Bernstein et al., 2004, Ishihara, 1995). The phase image $\phi(x,y)$ is obtained from:

$$\phi(x,y) = \tan^{-1}\frac{Im\{\hat{p}(x,y)\}}{Re\{\hat{p}(x,y)\}}, \qquad [1]$$

Since the inverse tangent function is bounded between$[-\pi,\pi]$, the phase image can only be mapped into this interval.

In a general MR acquisition, a phase image by itself is not useful since data are contaminated by system imperfections such as gradient eddy current or physical effects such as magnetic susceptibility (Haacke et al., 1999). For these reasons, phase images are generally represented by phase difference images plotting the differences between the phases of two sets of data, i.e. for image A and B that differ by the presence of a gradient lobe, for example, in order to negate everything except the phenomena under investigation, as described by the following function:

$$\phi(x,y) = \phi_A(x,y) - \phi_B(x,y). \qquad [2]$$

This phase can be used for shimming and correcting many MR nuances. However, one may also utilize the phase information to generate a contrast related to motion by intentionally introducing controlled motion artifacts into a phase image and studying

these phenomena related to motion by magnetic field gradient sensitization. Since the spins in a magnetic field possess a phase that is dependent on both the strength of the magnetic field and the applied magnetic field along the direction of the spin motion (Haacke et al., 1999), the phase equation can be correlated to the spin motion by:

$$\phi = \gamma \int_0^\tau \overrightarrow{B_0} \cdot \vec{r}(t)dt + \gamma \int_0^\tau \overrightarrow{G_E} \cdot \vec{r}(t)dt + \gamma \int_0^\tau \overrightarrow{G_r}(t) \cdot \vec{r}(t)dt, \quad [3]$$

where γ is the gyromagnetic ratio characteristic of the nuclei, $\overrightarrow{B_0}$ is the static magnetic field strength, $\overrightarrow{G_E}(t)$ is one of the encoding gradient vectors, $\vec{r}(t)$ is the spin motion vector, and $\overrightarrow{G_r}(t)$ is the MSG which is collinear to the encoding gradient and used for spin motion filtering (Muthupillai at al., 1995).

A cyclic induced displacement will cause a temporal spin motion vector governed by:

$$\vec{r}(t) = \overrightarrow{r_0} + \vec{\xi}(\vec{r}, t), \quad [4]$$

where $\overrightarrow{r_0}$ represents the initial location of the spin at time $t = 0$, and $\vec{\xi}(\vec{r}, t)$ is the cyclic displacement of the spin about its mean position caused by the actuator acoustic wave excitation.

If the MSG, with multiple bipolar pairs and duration τ , is synchronized at the same frequency with the induced spin motion , i.e., $\vec{\xi}(\vec{r}, t)$, and turned on for a duration τ so that $\int_0^\tau \overrightarrow{G_r}(t)dt = 0$, then the dynamic phase shift of the moving magnetization, i.e., equation [3] can be rewritten as:

$$\phi = \gamma \int_0^\tau \overrightarrow{B_0} \cdot \vec{\xi}(\vec{r}, t)dt + \gamma \int_0^\tau \overrightarrow{G_E} \cdot \vec{\xi}(\vec{r}, t)dt + \gamma \int_0^\tau \overrightarrow{G_r}(t) \cdot \vec{\xi}(\vec{r}, t)dt, \quad [5]$$

As explained previously in equation [2], while taking the difference between the phase images, the phase due to the static magnetic field and the encoding gradient is present and

assumed constant through toggled bipolar – reversed polarity− measurements and can be eliminated by the subtraction in equation [2]. However, the motion sensitization by the bipolar gradient can be set to be reversed and thus will be doubled in the subtraction. Therefore, only the third term of equation [5] remains and is used for motion detection:

$$\phi = \gamma \int_0^\tau \overrightarrow{G_r}(t) \cdot \vec{\xi}(\vec{r}, t) dt, \qquad [6]$$

The cyclic displacement vector $\vec{\xi}(\vec{r}, t)$ can be further written as:

$$\vec{\xi}(\vec{r}, t) = \overrightarrow{\xi_0}\, exp(j[\vec{k} \cdot \vec{r} - \omega t + \psi]), \qquad [7]$$

where $\overrightarrow{\xi_o}$ is the peak displacement of the spin from the mean position, $\vec{k}$ is the wave vector, ω is the angular frequency of the acoustic wave excitation, and ψ is the introduced phase offset between the bipolar gradient pulses and the acoustic wave.

Incorporating equation [7] into [6] and solving for equation [6] by choosing the integral of the dot product of the gradient vector and the position vector over τ to be zero, i.e., $\int_0^\tau \overrightarrow{G_r}(t) \cdot \overrightarrow{\xi}(\vec{r}, t) dt = 0$ and setting the bipolar gradient to be a sinusoidal wave, i.e., $\overrightarrow{G_r}(t) = \overrightarrow{G_0} \cos(\omega t)$, the equation is reduced to a phase constant that is a function of position and phase shift:

$$\begin{aligned} \phi(\vec{r}, \psi) &= \gamma \int_0^\tau \overrightarrow{G_0} \cos(\omega t) \cdot \overrightarrow{\xi_0}\, exp\left(j\left[\vec{k} \cdot \vec{r} - \omega t + \psi\right]\right) dt \\ &= \frac{\gamma \tau \left(\overrightarrow{G_0} \cdot \overrightarrow{\xi_0}\right)}{2} \cos\left(\vec{k} \cdot \vec{r} + \psi\right) \end{aligned} \qquad [8]$$

By examining equation [8], it becomes apparent that the measured phase magnitude is dependent on the duration (τ), the dot product of the amplitude of the bipolar gradient, and the peak displacement spin amplitude motion ($\overrightarrow{G_0} \cdot \overrightarrow{\xi_0}$) modulated by the cosine function. The dot product relationship indicates that the bipolar gradient acts as a filter

extracting its collinear displacement. It should also be noted that the phase difference depends on the shape of the bipolar gradients, such as rectangular (Muthupillai at al., 1995).

Two phase measurements are usually made by toggling the bipolar gradient pulses, positive to negative. The phase difference image is then calculated, either by subtraction or complex division, to give the shear wave image that reflects the phase shift caused by the propagating wave.

From the shear wave images, it is possible to extract the mechanical property called the shear elastic modulus (μ), which describes the proportionality relationship between lateral stress and strain in a material (Manduca et al., 2001). The speed of propagation (c) of shear waves in simple isotropic Hookean materials is related to the density (ρ) and the shear modulus by:

$$\mu = \rho c^2 = \rho(f\lambda)^2 \qquad [9]$$

The shear wave speed can be calculated from the wavelength (λ), which can be directly measured from the shear wave and the frequency of the externally applied mechanical excitation (f).

Hence, if the local wavelength is measured in an image depicting propagating shear waves, the shear modulus can be estimated. The calculation is further simplified by the generalization that the density of most biological soft tissues is the same as water (1000 kg/m^3) (Graff, 1999). This approach for estimating shear elasticity is clearly predicated on other simplifications, such as the assumption that the plane of section is parallel to the direction of wave propagation and that the mechanical properties of the tissue are approximately Hookean (non-viscous). The assumption holds merit since our

materials are assessed with induced motion of relatively small amplitudes (~100 μm). Recognizing that the latter assumption may be incorrect, the term shear stiffness is used to designate the quantity measured at a given shear wave frequency (Muthupillai et al., 1995). Shear wave images are collected at multiple phase offsets to calculate the stiffness in each voxel using an inversion algorithm (Oliphant et al, 2001). The resulting measurements at each pixel have been shown to strongly correlate (R^2>0.9914) with data collected using dynamic mechanical analysis, a common tissue testing device (Ringleb et al., 2005).

In a typical MRE system, the imaging pulse sequence controls the timing and acquisition in MRI. The spin movement can be measured in MRI using a phase contrast pulse sequence (Muthupillai at al., 1995). A simple gradient or spin-echo sequence can be modified to acquire the spin motion by synchronizing the actuator with the MSG (Muthupillai et al., 1995; Othman et al., 2005). The choice between the gradient- or spin-echo is based on the needed signal to noise ratio and homogeneity of the magnetic field. Gradient-echo based sequences are more favorable in low field or clinical scanners while spin-echo based sequences are more desirable at high field where the T_2 is shorter and there is a need for a more homogenous magnetic field.

The quality of MRE-derived localized information about a tissue's material is dictated by the spatial resolution. MRE has been performed in clinical MR systems, typically 1.5 T, with a voxel resolution of 1 mm x 1 mm x 10 mm. To achieve smaller voxel resolution requires a stronger magnet, i.e. 9.4T, and stronger magnetic field gradient with smaller and more sensitive RF coils that are capable of resolutions of less than 50 μm.

Long Term Goal

The long term goal of this research is to develop an MRE system capable of quantitatively monitoring the mechanical properties of tissue engineered materials both *in vitro* and *in vivo.* It is the intention that such a system will provide researchers with a noninvasive rapid-feedback method for improving the engineered outcome. Furthermore, a well designed MRE system will contribute to the body of knowledge concerning how differentiation, cellular contraction, scaffold remodeling, and biodegradation of the scaffold affect the morphological and mechanical environment of the construct over time. Such studies will enable the design of better engineered constructs that can be translated into treatment of tissue defects. Further extension of MRE includes the ability to provide a noninvasive feedback tool with which physicians and scientists can assess and respond to treatment without the need to remove the implanted material.

Objectives

Within the context of the long term goal, the position taken in this thesis is that MRE can be used to test tissue engineered materials *in vitro* and *in vivo* using a 9.4T MR scanner. As evidence to this point, the following chapters will demonstrate the application of MRE for testing constructs *in vitro,* establish a method for testing constructs implanted into mice, and provide quantitative assessment as to the development of the construct.

CHAPTER 2: MATERIALS AND METHODS

Introduction

In the following procedure, a 9.4 T MRE system was designed and implemented to evaluate the differentiation of bone marrow derived mesenchymal stem cells. In parallel to the development of the MRE system, differentiation was validated with a cellular monolayer before progressing to construct development. After the monolayer study, cells of the same passage were seeded onto gelatin scaffolds. Both mouse and human origin cells were differentiated by application of differentiation reagents and assessed with MRI and MRE through the use of a modified spin-echo sequence coupled with a piezoelectric actuator. After four weeks of *in vitro* study, the constructs were implanted and observed in an athymic mouse model. Figure 2 shows an illustrative timeline of the tissue monitoring process for both the i*n vitro* and *in vivo* study. All procedures were approved by the University of Nebraska-Lincoln Institutional Animal Care and Use Committee and Institutional Biological Safety Committee.

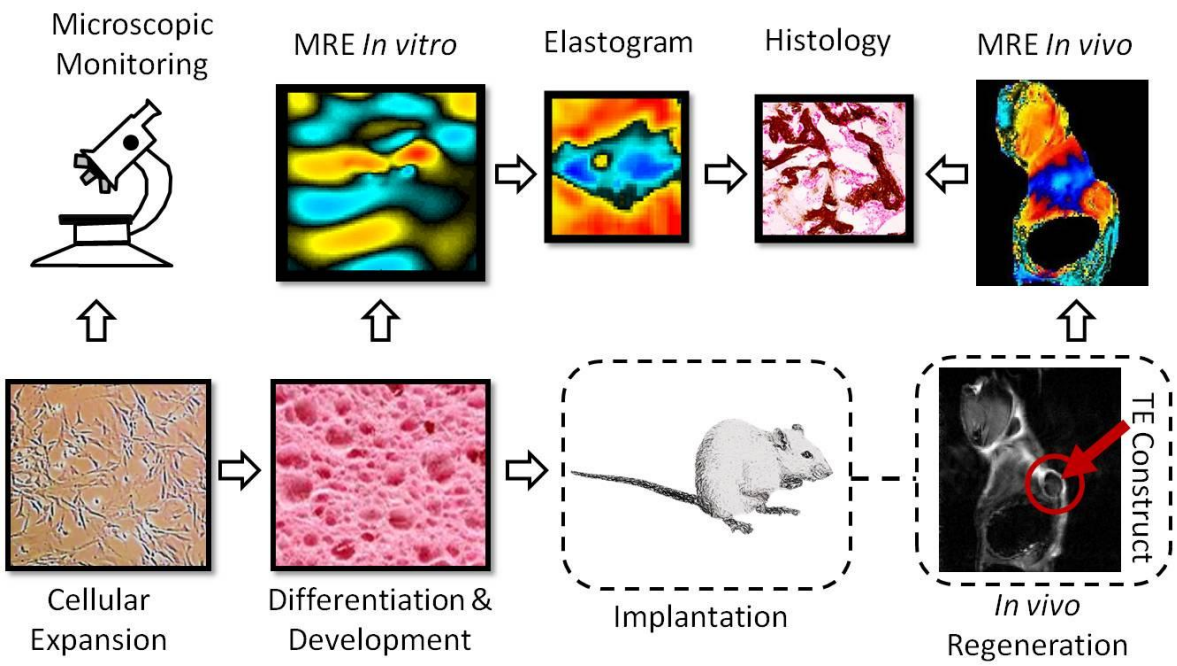

Figure 2. Timeline of tissue monitoring process with MRE. After removing from cryopreservation, the cells are monitored using a microscope throughout expansion. Once the cells were seeded onto the scaffold and differentiation reagents were applied, the constructs were monitored using MRI for four weeks. After *in vitro* development the constructs were implanted into mice. The mice were evaluated using MRI and the stiffness measurement technique of MRE. Differentiation was also evaluated via stain of extracted tissues.

Cell Culture

Mesenchymal stem cells (MSCs) obtained from adult human bone marrow (PT-2501, Lonza, Walkersville, MD) and mouse bone marrow (D1ORLUVA, ATCC, Manassas, VA) were purchased from their respective companies. The human MSCs (hMSCs) were expanded in the Lonza recommended mesenchymal stem cell growth media (MSCGM™, PT-3001, Lonza) supplemented with L-glutamine. Mouse MSCs (mMSCs) were expanded in Dulbecco's Modified Eagle Medium (DMEM, ATCC) with 10% (v/v) fetal bovine serum (FBS, Invitrogen, Carlsbad, CA) and 1% (v/v) antibiotics (PenStrep, Invitrogen). Both cell types were incubated at 37 °C with 5.0 % CO_2 and expanded to the populations essential for the respective study.

- **Differentiation Monolayer**

Differentiation of the human mesenchymal stem cells was performed by seeding the cells at $3x10^3$ cells/ cm^2 for osteogenic differentiation and $2.5x10^4$ cells/ cm^2 for adipose (McBeath et al., 2004). Osteogenesis was induced with the use of the hMSC Osteogenic Differentiation Bullet Kit (PT-3002, Lonza). The kit consisted of osteogenic basal medium, dexamethasone, ascorbate, growth supplements, L-glutamine, penicillin/streptomycin, and β-glycerophosphate.

For differentiation of hMSCs into adipocytes, an hMSC Adipogenic Differentiation Bullet Kit (PT-3004, Lonza) was applied once cells appeared confluent in the well. The kit consisted of adipogenic induction medium, recombinant h-insulin, dexamethasone, indomethacin, isobutyl-methylxanthine and L-glutamine. After three days, the induction media was replaced with adipose maintenance media with recombinant h-insulin and L-glutamine for 24 hours then return to induction media. The

cycle was repeated three times and then exchanged only in maintenance media every two days.

Osteogenesis was validated through the use of a von Kossa silver stain counter stained with neutral red. Von Kossa was applied to examine the mineralization during differentiation due to calcium deposition of the extracellular matrix (Hong, 2005). To assess adipogenesis, oil red O was applied to label the formation of lipids. Assessment of the stains was conducted using a VWR VistaVision inverted microscope retrofitted with a Microsoft ® LifeCam web camera for image acquisition.

- **Construct preparation**

Prior to evaluation with human mesenchymal stem cells, constructs were produced using mMSCs. Biodegradable sterile gelatin sponge scaffolds (Gelfoam®, Baxter Healthcare Corporation, Hayward, CA) were trimmed using a razorblade into 4x4x3.5 mm^3 pieces and pre-wet in growth media (DMEM, ATCC). The mMSCs were then seeded onto the constructs at a concentration of $1x10^6$ cells/ mL of suspension. To decrease air bubbles in the construct as well as improve seeding a 20 ml syringe applied a slight vacuum to each vial (Dennis, 1992). After 24 hours of incubation, osteogenic differentiation media consisting of DMEM (ATCC), 50 μM L-ascorbic acid-2-phosphate (Sigma-Aldrich, St. Lois, MO), 10 mM β-glycerophosphate (Sigma), and 100 nM dexamethasone (Sigma) was added and exchanged every two days (Marion and Mao, 2006).

For preparation of the hMSC constructs, biodegradable sterile gelatin sponge scaffolds were trimmed using a biopsy punch into 4 mm diameter, 3.5 mm thick pieces and pre-wet in growth media (MSCGM, Lonza) for one hour before seeding. Next,

hMSCs were seeded onto the scaffolds at a density of $1x10^6$ cells/ mL for osteogenic constructs and 3×10^6 cells/ mL for adipogenic constructs with the help of slight vacuum generated by a 20 ml syringe (Dennis, 1992). Then, the scaffold-cell suspension was incubated at 37 $^{\circ}$C for two hours (Hong, 2005) before transfer to growth media for 24 hours.

Differentiation was induced the following day (Hong, 2005) for osteogenic constructs by culturing in osteogenic differentiation media (Lonza), which was exchanged every two days. For differentiation of hMSCs into adipocytes, adipose induction media (Lonza) was applied three days after seeding onto the scaffold with the intension of differentiating after cells had reached confluence. After three days, the induction media was replaced with adipose maintenance media (Lonza) for 24 hours then return to induction media. The cycle was repeated three times and then exchanged only in maintenance media every two days.

MRE *in vitro*

- **MRI/ MRE system**

In vitro MRI experiments were conducted at 9.4 T (400 MHz for protons) using an 89 mm vertical bore magnet equipped with triple axis gradients (maximum strength 100 G/cm) (Agilent, Santa Clara, CA). Measurements were acquired using a 1 cm Litz RF volume coil (Doty Scientific, Columbia, SC) to transmit and receive the nuclear magnetic resonance signals.

For MRE experiments, a modified phase contrast pulse sequence was written and integrated with the imaging software, VnmrJ 2.3A, enabling the user to select the MRE parameters. These parameters included gradient amplitude (0-100 G/cm), actuator

frequency, delay between the mechanical actuator and the bipolar gradient, MSG direction, and number of bipolar pairs.

For all experiments, a piezoelectric bending actuator (Piezo systems, inc., Woburn, MA) provided the displacement for the system and was synchronized with the phase contrast imaging pulse sequence. The actuator was driven by a signal generator (Tektronix, Beaverton, OR) in line with a linear amplifier (Piezo). To improve coupling between the actuator and the sample media of interest, a small tip approximately the size of a serial port pin was soldered to the non-fixed end of the actuator beam.

- **Actuator Characterization**

In order to provide optimal displacement to the system, actuator characterization was performed using a Laser Doppler Vibrometer (Polytec, Dexter, MI) as illustrated in Figure 3. For MRE testing of the samples, a tissue construct was placed in a 10 mm test tube and enclosed in 0.5% agarose gel to promote the transfer of motion through the construct. By shining the laser beam onto the surface of the actuator, the reflected signal will indicate the actuator's velocity or displacement. Characterization of the actuator enables tailoring the actuator to deliver maximum displacement under loaded conditions. Identification of the optimal frequency is achieved by driving the actuator at 20 Vpp with white noise input sweeping from 0.02-2 kHz in 10 ms cycles. Then, analysis of the characterized actuator velocity reveals the loaded systems resonance frequency. After identification of the resonance frequency, the signal generator was then used to drive and observe the displacement of the actuator at the specific frequencies at 200Vpp. Once completed, the frequency with greatest displacement was the one selected for use in the

MRE experiment. Depending on loading and condition of the actuator, driving frequencies were around 500-700Hz with displacements of ~200 microns.

- **Imaging Procedure**

Adipogenic, osteogenic, and undifferentiated (control) constructs were monitored at five points of growth (week 0, 1, 2, 3, and 4). Constructs were first quantified in terms of their spin-lattice (T_1) and spin-spin relaxation (T_2) properties as well as diffusion (ADC).

T_1 measurements were performed with multiple-echo multiple-slice sequence in which the repetition time was exponentially arrayed in 12 steps from 0.05 to 4 s with a single echo time of 8.72 ms, slice thickness of 1 mm, and spatial resolution of 78 µm x 78

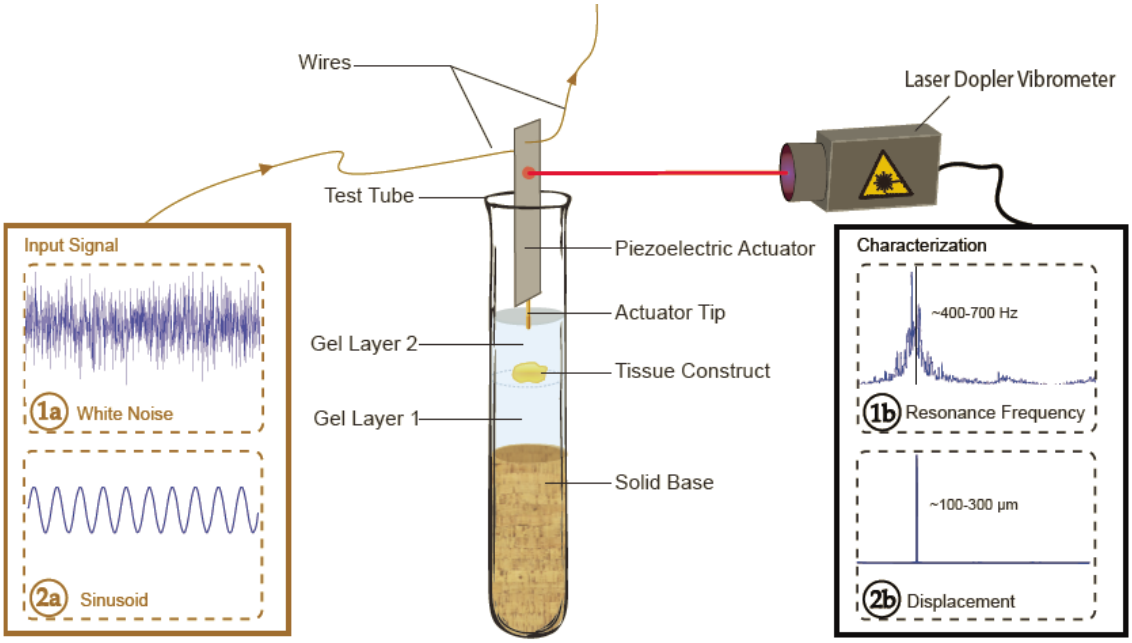

Figure 3. Actuator characterization procedure. To determine the frequency response of the actuator, a white noise is first sent into the system (1a) and the resulting motion is detected using a Laser Doppler Vibrometer (1b). Once the resonance frequency is detected, a continuous sinusoid signal at resonance (2a) is sent to for determining the displacement (2b) being transferred to the construct environment.

μm. Each slice was taken through the center of the construct. T_2 measurements were acquired using the same sequence as the T_1 measurements only with a repetition time fixed at 4 s and echo times evenly spaced from 10 to 320 ms in 32 steps. Furthermore, the apparent diffusion coefficient (ADC) was measured using a diffusion weighted image with the diffusion gradient encoding along the readout direction. The 'b' values of each of the 14 steps linearly corresponds to diffusion-weighted gradient strength (repetition time , 1 s; echo time, 27.65ms; separation (δ), 3 ms; difference (Δ), 18 ms; spatial resolution, 78 μm x 78 μm, averages, 1; and 14 'b' values up to 2000 s/mm^2). MR property values were calculated from the data using a least-squares single exponential fitting method using MATLAB 2009b (MathWorks, inc., Natick, MA).

Standard spin echo images were acquired for each construct. Osteogenic images and respective controls were obtained with repetition time, 1 s; echo time, 50 ms; slice thickness, 1; averages, 8; spatial resolution, 78 μm x 78 μm. Adipogenic constructs and respective controls were evaluated with the following parameters: repetition time, 1 s; echo time, 80 ms; slice thickness, 1; averages, 8; spatial resolution, 78 μm x 78 μm.

MRE acquisitions were conducted at the frequency determined by the Laser Doppler Vibrometer. For the use of directional filtering, eight offsets were acquired. Typical parameters for an MRE acquisition were repetition time, 1 s; echo time, 25.5 ms; slice thickness, 1;spatial resolution, 78 μm x 78 μm; actuator frequency, 730 Hz, bipolar pairs, 4. It should be noted that for MRE the echo time is dependent upon the number of bipolar pairs and the period of the actuator frequency; hence, echo time is minimized in order to minimize the effects of T_2 relaxation and maximize the available signal.

- **Processing**

Following the collection of the motion encoded images, the files were load into MATLAB and complex division was performed on the positive and negative datasets. The resulting shear wave images were then saved as .mat files and transferred to a MATLAB script developed by Mr. Thomas Boulet, in which the three-dimensional dataset (two spatial, one temporal) was used to derive the localized stiffness of the tissue construct The algorithm approximates spatial second derivatives with finite difference and computes the shear modulus on a pixel-by-pixel basis. From this complex number, many mechanical parameters can be deduced such as the shear wave speed, wave attenuation, shear stiffness, shear elasticity, shear viscosity, etc. The algorithm also allows the selection of regions of interest from which the mean and standard deviation of each parameter is calculated.

- **Histological analysis**

After completion of the study, the tissue constructs were then placed in 10% formalin and transferred to either the University of Nebraska-Lincoln Veterinary Diagnostic Laboratory (Lincoln, NE) or Histoserv, inc. (Germantown, MD) for histology. Constructs were then paraffin embedded and sectioned. Morphology of each construct was evaluated after the application of hemotoxylin and eosin staining and if enough sample remained, stains such as oil red O or von Kossa were performed.

Animal Model MRE

- **Tissue implantation**

Following four weeks of *in vitro* culture, constructs were implanted in eight week old male nude immunodeficient mice (nu/J, The Jackson Laboratory, Bar Harbor, ME). For the implantation surgery, the mouse was anesthetized with ketamine and xylazine at a dose of 90 mg/kg and 10 mg/kg, respectively. The surgical site was disinfected with betadine and isopropyl alcohol. A 20 mm incision was made mid-sagittal across the dorsum in the lower lumbar region where a subcutaneous pocket was created on the right side of the midline using blunt dissection. Tissues were then implanted as shown in Figure 4. Following surgery, the animals were allowed to heal for two weeks before removing the suture and conducting MRE testing.

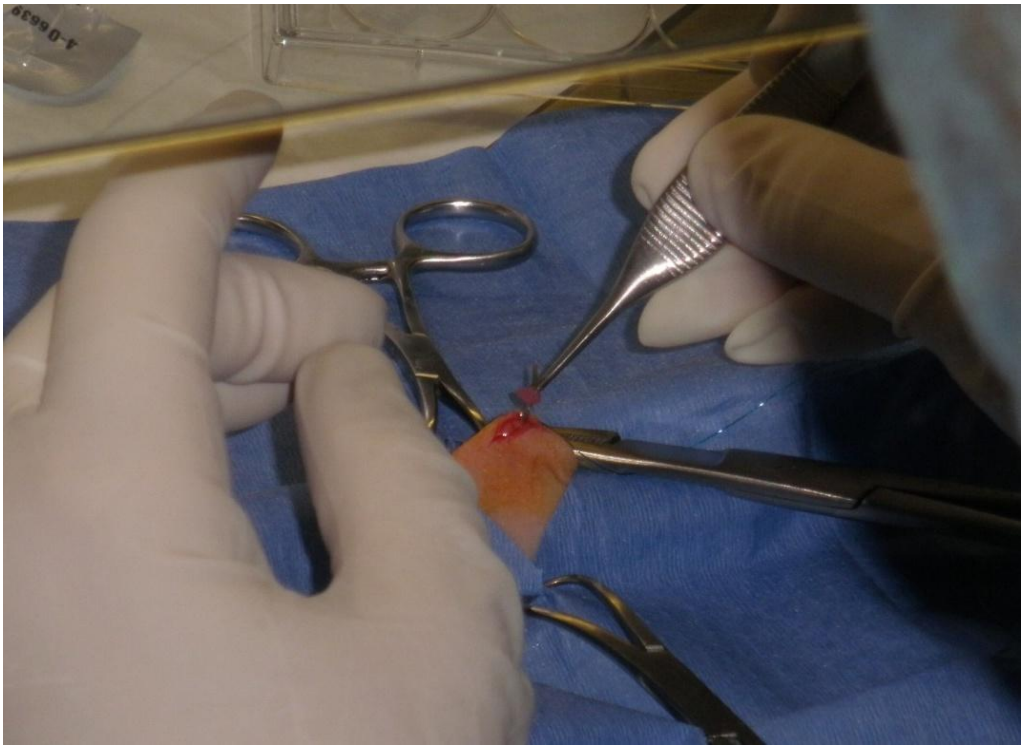

Figure 4. Implantation of a tissue into the subcutaneous of an athymic mouse. Athymic mice are used in order to reduce the occurrence of immune response.

- **MRE System**

All *in vivo* MRE scans were conducted with a 4cm Millipede® RF coil (Agilent) for transmission and reception of the nuclear magnetic resonance signals. Furthermore, an actuator was developed to accommodate the geometry of the mouse and provide sufficient displacement into the TE construct without disrupting the skin's surface. The design was achieved through the use of an adjustable beam design which permits the actuator to be rotated over the curvature of the mouse's body as shown in Figure 5. (For a more on the *in vivo* actuator designs see Appendix A). The mice were placed in ventral recumbency onto the animal positioning unit and the actuator attachment was placed adjacent to the tissue.

Prior to placement in the magnet, the MRE actuator system was characterized using the Laser Doppler Vibrometer and the optimum operating frequency was

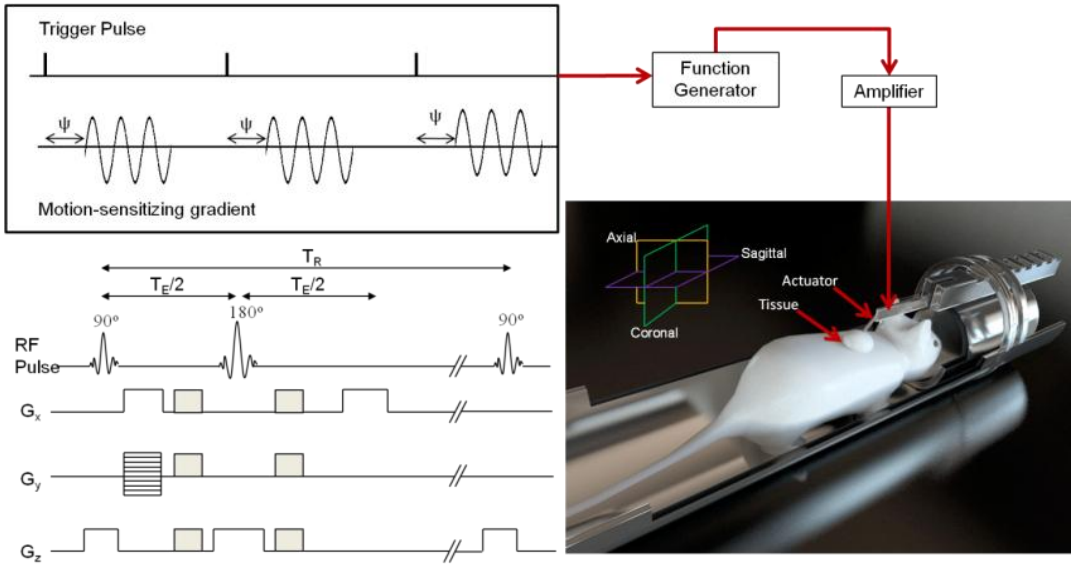

Figure 5. Experimental setup for *in vivo* MRE and corresponding pulse sequence. The actuator was designed to be placed next to the construct for maximum wave propagation. determined in the same manner described for *in vitro* actuator characterization.

Additionally, for all uses in which the actuator was active and in contact with the mouse, sedation was kept at greater that 1.5 % isoflurane and breathing rate was less than 75 breaths per minute for the health and wellbeing of the animal. During the MR experiment, the mice were kept anesthetized with 1-2% isoflurane (Molecular Imaging Products Company, Bend, OR) and monitored (Small Animal Instruments, inc., Stony Brook, NY). Monitoring and gating capabilities included the use of ECG, respiration, and pulse oximetry. The body temperature was assessed using a temperature probe and adjusted via an air heater. Each imaging session was approximately 2 hours per mouse.

- **Imaging Procedure**

Once the tissue location was identified, fast-spin or spin-echo images of the construct were acquired in addition to the MRE measurements. MRE acquisition was performed in the same manner as *in vitro* MRE with the addition of external respiration triggering to reduce motion induced artifacts. To reduce the amount of time the mouse spent in the magnet, multiple phase offset videos were acquired at four to six offsets rather that the eight that had been acquired in the *in vitro* study. Both mMSCs and hMSCs were implanted into mice in separate studies.

- **Histological Analysis**

The mMSC constructs were retrieved eight weeks after implantation and fixed with 10% neutral buffered formalin. Constructs were sent for analysis to University of Nebraska-Lincoln Veterinary Diagnostic Laboratory (Lincoln, NE) or HistoServ, inc. (Germantown, MD). The tissues were then paraffin embedded and stained with hematoxylin and eosin and von Kossa to identify morphology and examine calcium deposition.

CHAPTER 3: RESULTS

In vitro

- **Monolayer**

Validation of hMSC monolayer differentiation was performed using oil red O and von Kossa. Figure 6 (a-d) shows the increasing number of lipids being produced for four weeks of differentiation. Each image from left to right was acquired in one week increments. In Figure 6 (e-g) the black regions are the indications of calcium deposition and the red regions are either collagen or osteoid. No week four data of the osteogenic induced cells was acquired due to delamination of the cells from the well's surface. The monolayer study confirmed that the hMSCs were capable of differentiating toward both the adipogenic and osteogenic pathways.

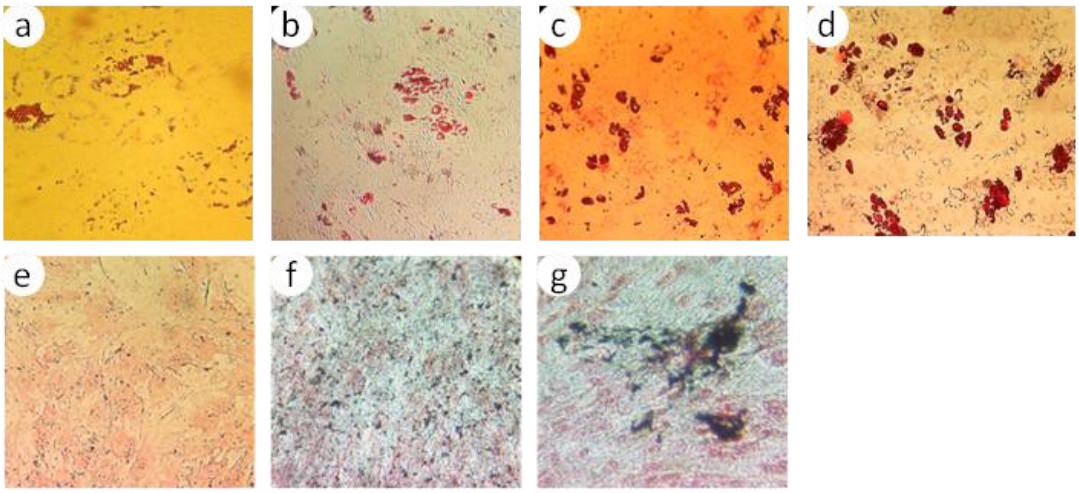

Figure 6. Evaluation of hMSC differentiation on a monolayer. The adipogenic differentiation was evaluated over weeks 1-4 (a-d) through the use of oil red O to stain lipids red. An increasing presence of lipids provided indication that cells were treated with adipogenic reagents were indeed differentiating toward adipocytes. Mineralization, a byproduct of osteogenesis was evaluated for weeks 1-3 (e-g) with von Kossa. All images were acquired at 250X.

- **MR Properties**

The axial spin-echo images of the adipogenic and osteogenic constructs over four weeks of differentiation are shown in Figures 7 and 8. At the conclusion of the four week study the osteogenic constructs were the smallest in diameter and also had less signal intensity than the undifferentiated controls. Conversely, the constructs directed toward adipogenesis, after an initial reduction in size, appeared to be increasing in construct size as well as intensity. Figure 9 shows the changes in the relaxation times spin-lattice, spin-spin relaxation times and the apparent diffusion coefficient for the four weeks of differentiation (n=3). From the beginning of the study to the end at week 4, the osteogenic constructs for T_1 decreased 8%, starting at 1.42±0.04 s to 1.30±0.02 s after four weeks; T_2 decreased 14%, starting at 100.7±8.8ms to 86.3±6.2 ms; and ADC decreased by 11% for week zero to week 3. For the adipose constructs T_1 decreased by < 2%, T_2 increased by 5% starting at 94.8±7.6 ms to 99.7±4.8 ms; and ADC experienced change of < 1%.

- **MRE sequence testing**

Testing of the MRE sequence provided the first evidence of the detection of shear waves using a vertical bore 9.4T system. Figure 10 displays the displacement map as well as the derived elastogram. The top layer of 1.0% agarose gel was determined to have a shear stiffness of ~20 kPa and the 0.5 % base was ~5 kPa. The sequence was capable of encoding motion along the read, slice, and phase encoding gradient directions.

- ***In vitro* MRE**

Figure 11 shows the construct development map over a four week period. Adipogenic (A) and osteogenic (O) constructs are shown from left to right with

corresponding magnitude and shear wave images, elastogram, and average shear stiffness. The colormap for the elastogram corresponds with the color scheme of the bar chart. While both seeded sponges started at approximately 3 kPa, osteogenic directed tissues resulted in a stiffness of 22 kPa; whereas, adipose directed tissues decreased in stiffness to 1 kPa. Furthermore, the osteogenic constructs showed a notable decrease in size in comparison from beginning to end of the study as was previously noted in the magnitude acquisitions. In addition to the shear stiffness properties derived using the inverse problem, shear elasticity and shear viscosity are reported in Table 1.

- **Histology**

Hematoxylin and eosin stained constructs revealed the morphology of the assessed constructs. Figure 12 shows the material after four weeks with a magnification of 400X. The osteogenic construct had greater apparent cellularity in comparison to the adipogenic. Also lipid vacuoles were identified in the adipogenic construct providing evidence of differentiation on the construct. Prior to implantation, week 4 constructs were evaluated with von Kossa and oil red O stains and confirmed differentiation, which is presented in Figure 13.

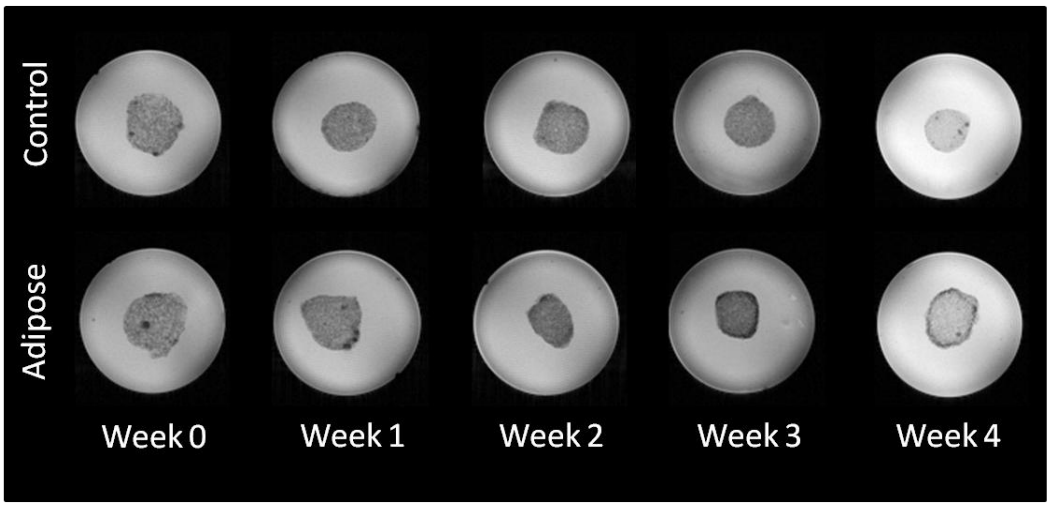

Figure 7. Adipogenic construct spin echo images. Axial images of control (top row) and engineered constructs undergoing adipogenic differentiation (bottom row) over four weeks of incubation. Undifferentiated constructs seeded at the same density as the adipogenic constructs decreased in diameter through the four weeks of study. Images parameters are as follows: spin-echo sequence; repetition time, 1 s; echo time, 80 ms; slice thickness, 1; averages, 8; field-of-view, 1.0 cm x 1.0 cm; spatial resolution, 78 μm x 78 μm.

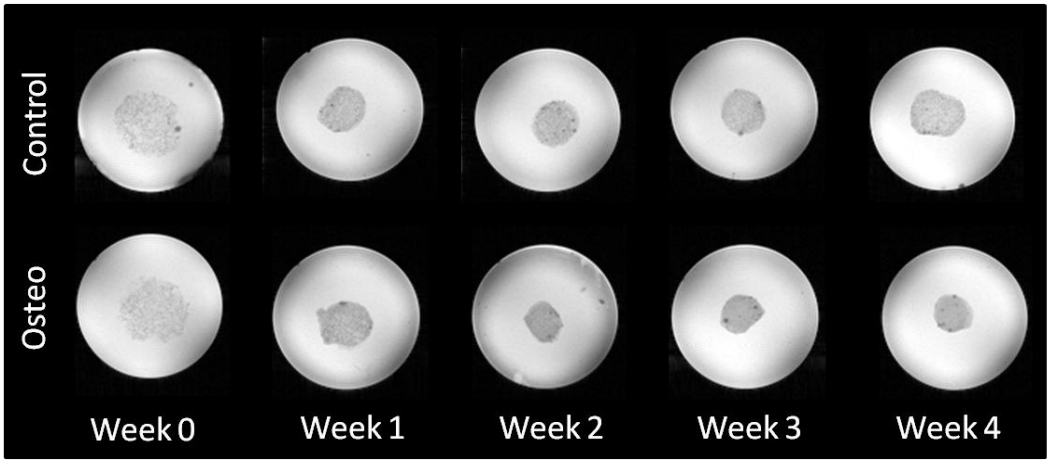

Figure 8. Osteogenic construct spin echo images. Axial spin echo images of control (top row) and engineered constructs undergoing osteogenic differentiation (bottom row) over four weeks of incubation. Image parameters are as follows: spin-echo sequence; Repetition time, 1 s; echo time, 50 ms; slice thickness, 1; averages, 8; field-of-view, 1.0 cm x 1.0 cm; spatial resolution, 78 μm x 78 μm.

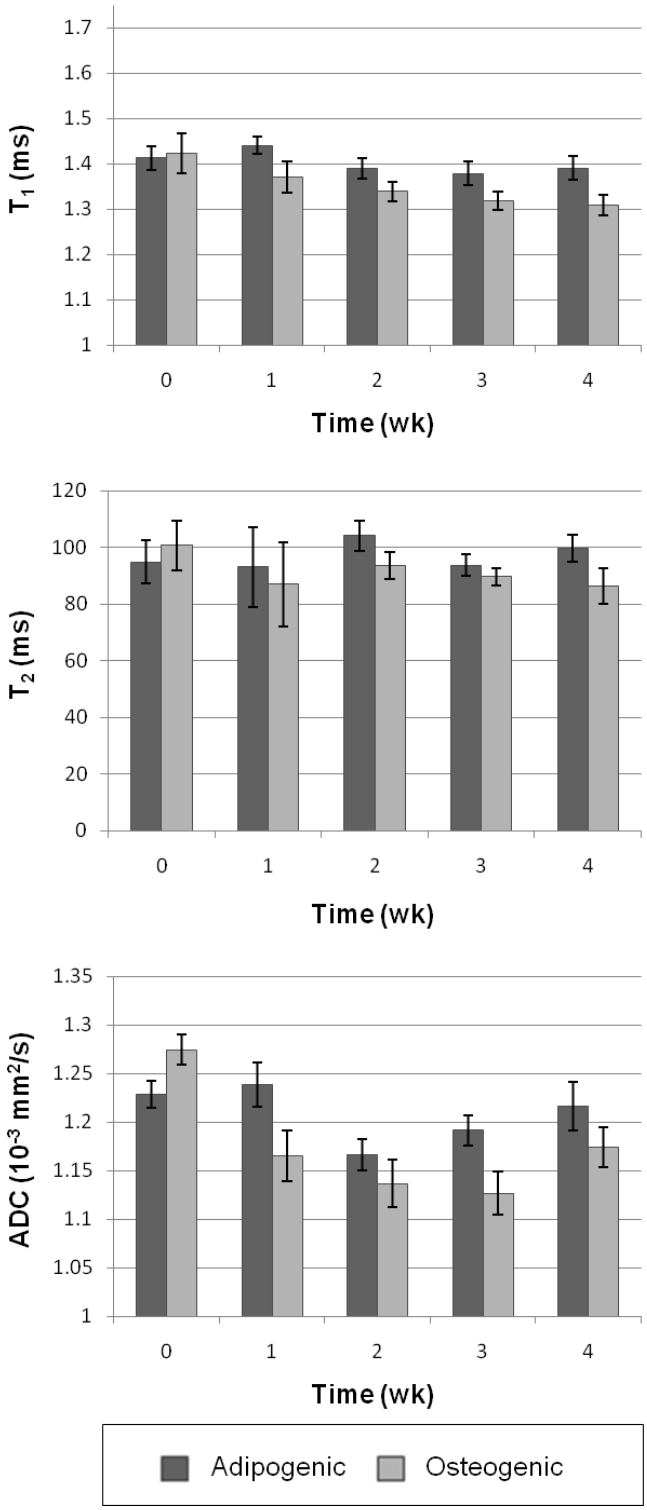

Figure 9. Graphs of the MR properties: T_1, T_2 and ADC for adipogenic and osteogenic constructs over four weeks of tissue development. Mean and standard deviation were determined using a selected ROI for each image (n=3).

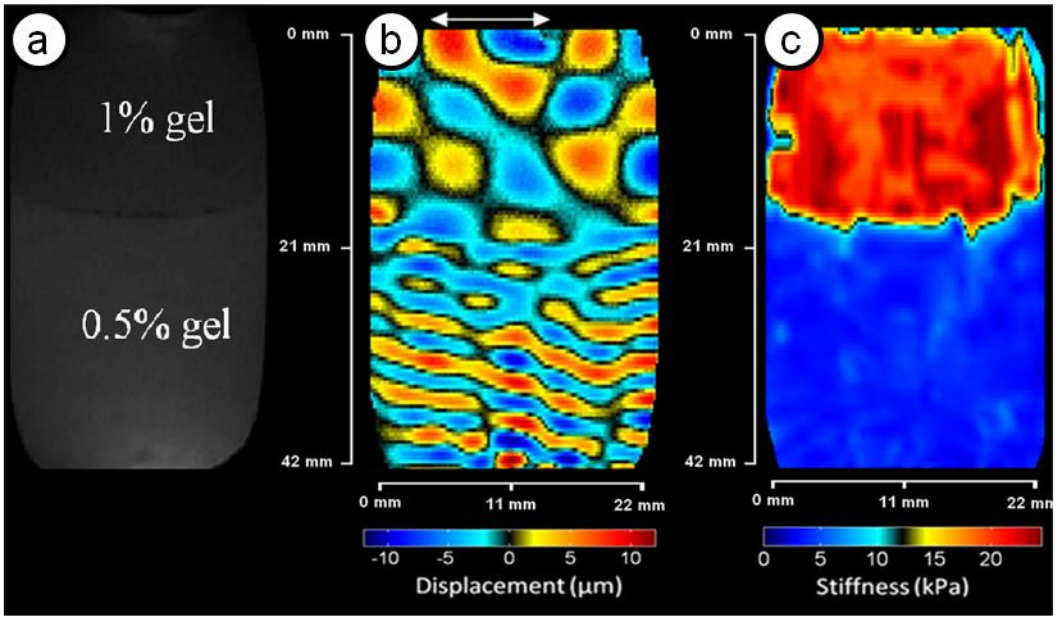

Figure 10. Demonstration of MRE shear wave. A two layer agarose gelatin phantom with magnitude (a) and corresponding shear wave (b) image. The resulting elastogram (c) was derived using an inverse problem algorithm. A piezoelectric actuator driven at 600 Hz was placed on the top of the gel phantom. Images parameters are as follows: MRE spin-echo sequence; repetition time, 1.2 s; echo time, 41.19 ms; slice thickness, 1 mm; averages, 1; field-of-view, 5.0 cm x 2.5 cm, in-plane resolution = 390 μm x 195 μm, gradient amplitude = 45 G/cm, actuator frequency, 600 Hz; bipolar pairs, 8.

Table 1. Mechanical properties of adipogenic and osteogenic constructs over a four week period of growth.

		Week 0	Week 1	Week 2	Week 3	Week 4
Stiffness (kPa)	Adipogenic	3.28 ± 1.03	2.22 ± 0.99	2.51 ± 0.91	1.94 ± 0.76	1.19 ± 0.55
	Osteogenic	3.06 ± 0.45	8.34 ± 1.29	8.91 ± 1.28	12.15 ± 0.88	22.11 ± 1.46
Shear elasticity μ1 (kPa)	Adipogenic	2.51 ± 0.94	1.76 ± 0.69	1.55 ± 0.67	1.08 ± 0.46	0.68 ± 0.30
	Osteogenic	1.57 ± 0.35	4.37 ± 1.68	5.58 ± 1.48	8.22 ± 2.02	12.77 ± 3.17
Shear viscosity μ2 (Pa.s)	Adipogenic	0.43 ± 0.14	0.23 ± 0.14	0.17 ± 0.07	0.11 ± 0.08	0.10 ± 0.04
	Osteogenic	0.36 ± 0.07	0.74 ± 0.22	0.81 ± 0.20	0.71 ± 0.22	2.02 ± 0.37

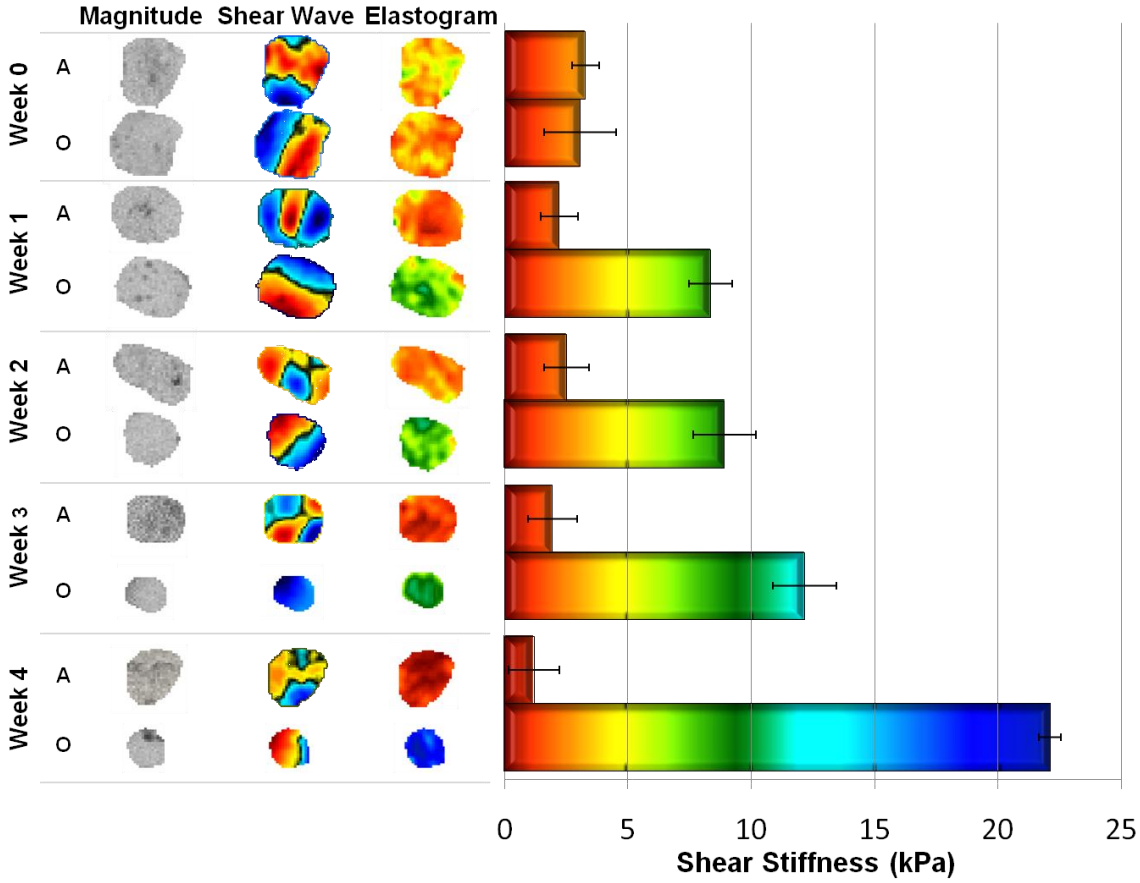

Figure 11. Construct development map over four week period. The hMSC adipogenic (A) and osteogenic (O) constructs are shown from left to right with corresponding magnitude image, shear wave image, elastogram, and average shear stiffness. The frequency of assessment for all the constructs was approximately 720 Hz. The standard error bars are for the standard deviation of shear stiffness within the region of interest of the elastogram.

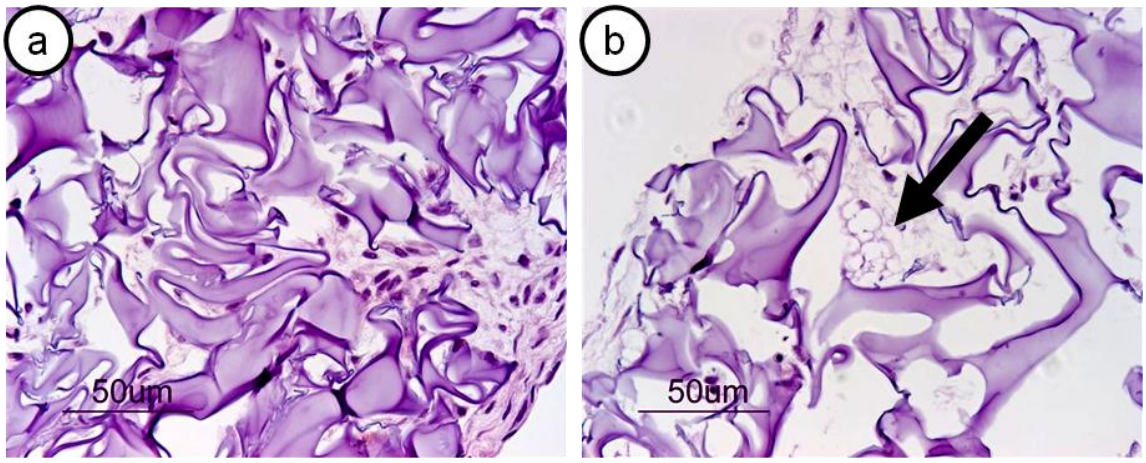

Figure 12. *In vitro* evaluation using hematoxylin and eosin stain. Osteogenic (a) and adipogenic (b) constructs were produced from undifferentiated hMSC. The hMSCs ere differentiated with adipogenic and osteogenic reagents and assessed after four weeks of *in vitro* growth. In (b) the arrow is identifies the lipid vacuole of a mature adipocyte.

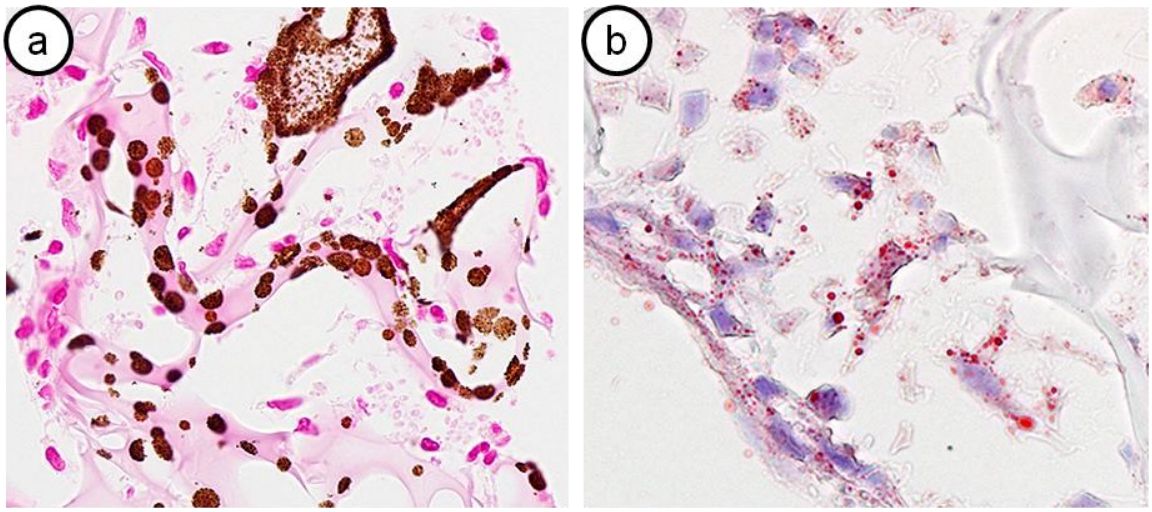

Figure 13. Von Kossa and oil red O stains of differentiated mMSCs. Following four weeks of i*n vitro* differentiation, von Kossa (a) was conducted for identification of calcium deposition. Oil red O (b) was applied to adipogenic constructs to identify the presence of lipids with adipogenic cells. Lipids are the reds spheres shown in red on the purple matrix. Magnification 400X (Histoserv).

In vivo

- **Magnitude Images**

Following evaluation of the constructs *in vitro* and implantation of the tissues into the athymic mice, MR magnitude and shear wave images of the constructs were acquired at different growth periods. Figure 14 shows an osteogenic construct four weeks after implantation. A comparison of constructs with the same acquisition parameters is shown in Figure 15. The osteogenic constructed had a measured diameter of 1.7 mm whereas the adipogenic construct had a diameter of 3.2 mm.

- **MRE**

Figure 16 shows MRE shear waves through an osteogenic construct followed by von Kossa staining indicating the presence of calcium. Shear wave images for the construct and neighboring temporal muscles are shown in Figure 16 with phase delays of $\frac{\pi}{2}$ and $\frac{3\pi}{2}$ with corresponding magnitude image. Half a wavelength was attained in the temporal muscle, with stiffness of 15kPa. To better visualize the shear wave in the construct, a close up is shown of the two phase delays where the measured amplitude motion was up to 80 micron as shown in the horizontal line profile. Half a wavelength was not attained in the construct; hence, no stiffness estimation could be performed. In contrast to the osteogenic constructs, Figure 17 shows the presence of multiple waves in an adipogenic construct. The measured stiffness of the construct was 4.2±0.9 kPa.

- **Histology**

After eight weeks of *in vivo* testing a construct was excised from the host mouse and assessed with hematoxylin and eosin staining. The confirmation of the bone differentiation is shown in Figure 18.

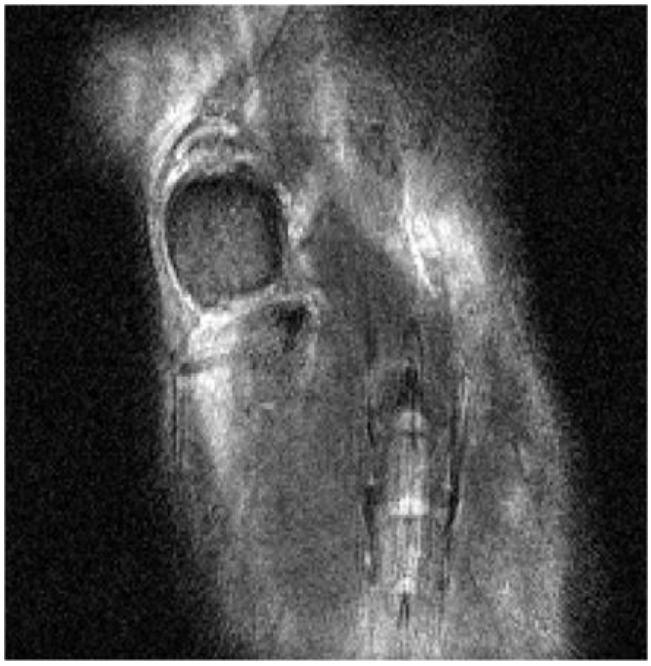

Figure 14. Osteogenic construct after four weeks of incubation. The mMSC based construct is approximately 3 mm in diameter. Fast spin-echo multiple slice sequence: repetition time, 2 s; echo trail length, 4; echo spacing, 10 ms; field-of-view, 2.5 cm x 2.5 cm; matrix size, 256 x 256; slice thickness, 1.0 mm; averages, 4.

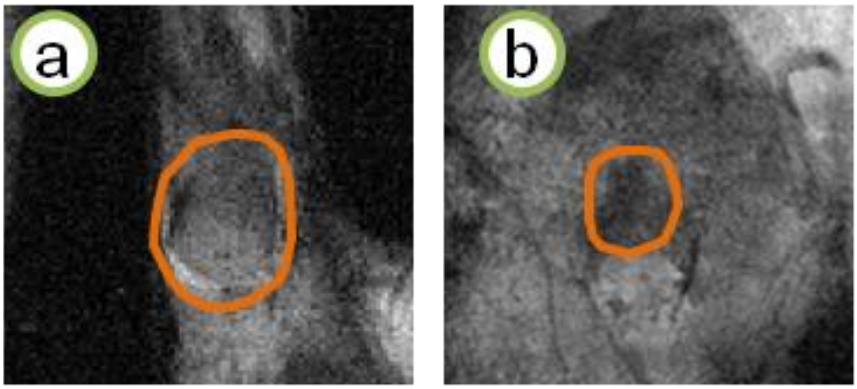

Figure 15. Constructs two weeks after implantation. The hMSC adipogenic (a) and osteogenic (b) are circled showing that the adipogenic construct is approximately three times larger than the osteogenic construct. Multiple echo multiple slice sequence: repetition time, 1 s; echo time, 9.27 ms; field-of-view, 2.0 cm x 2.0 cm; slice thickness, 1.0 mm; matrix size, 256 x 256; averages, 4.

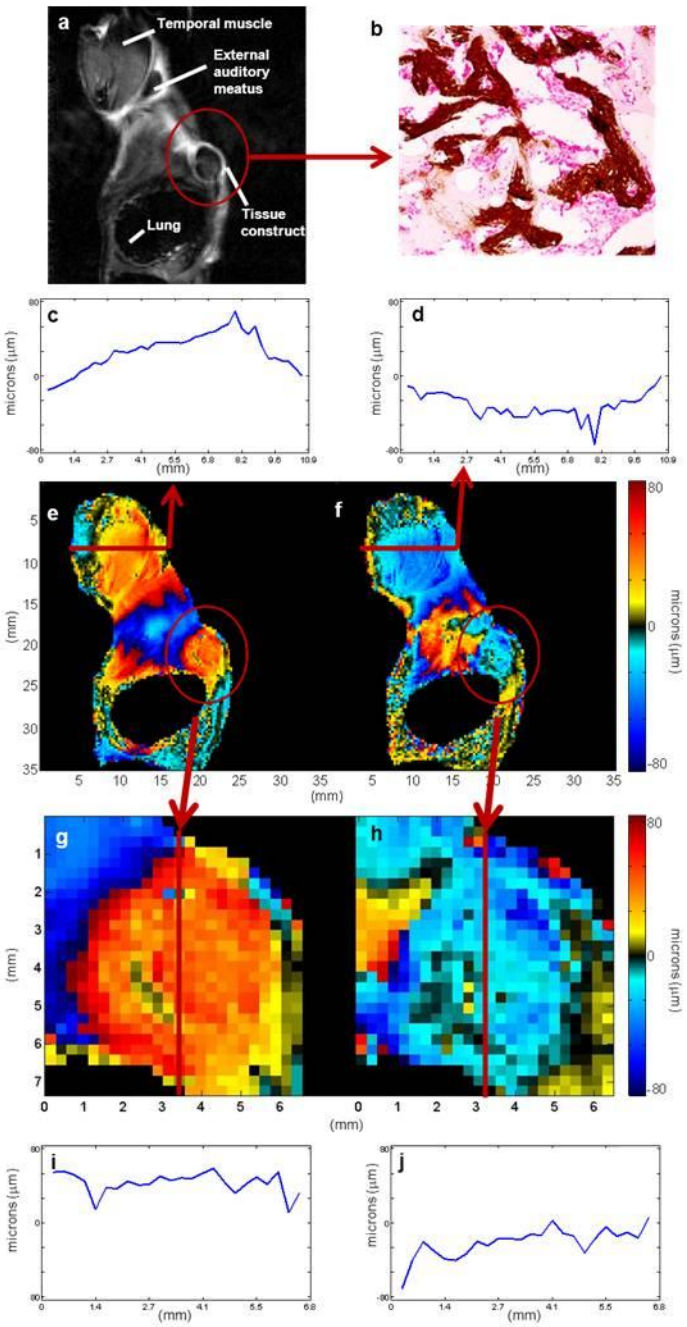

Figure 16. Osteogenic construct imaged four weeks post implantation. Shear wave images of an osteogenic mMSC construct were acquired with delays of π/2 (c,e,g,i) and 3π/2 (d,f,h,j) with the corresponding MR coronal image shown in (a) and hematoxylin and eosin staining (b). Close up of the TE construct shows the propagation of the wave with different delays. Shear wave through the temporal muscle (e,f) produced recorded a shear stiffness of 15kPa.

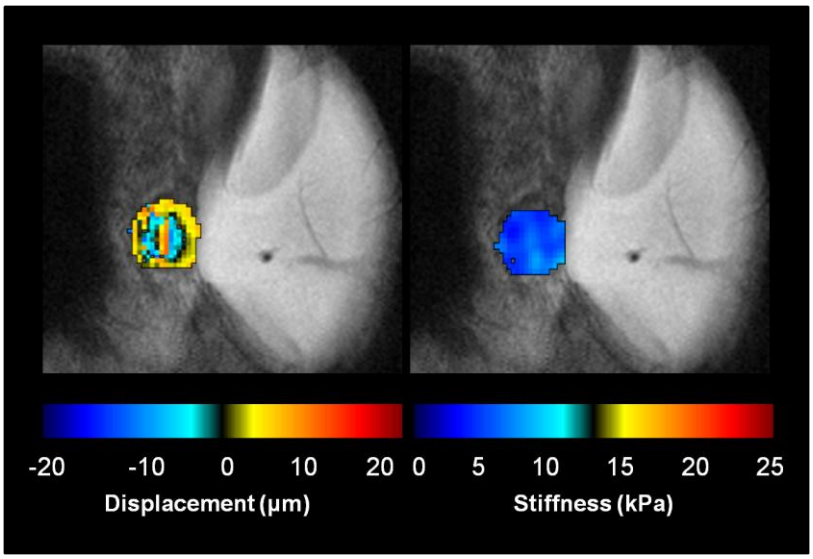

Figure 17. Shear wave taken through an adipogenic construct. From the shear wave (left), the hMSC adipogenic construct had measured shear stiffness (right) of 5 kPa. MRE spine-echo sequence: repetition time, 1 s (externally triggered); echo time, 32.01 ms; field-of-view, 2.4 cm x 2.4 cm; slice thickness, 1 mm; matrix size, 128 x 128, averages, 2; actuator frequency, 915 Hz, gradient amplitude, 90 G/cm; bipolar pairs, 8.

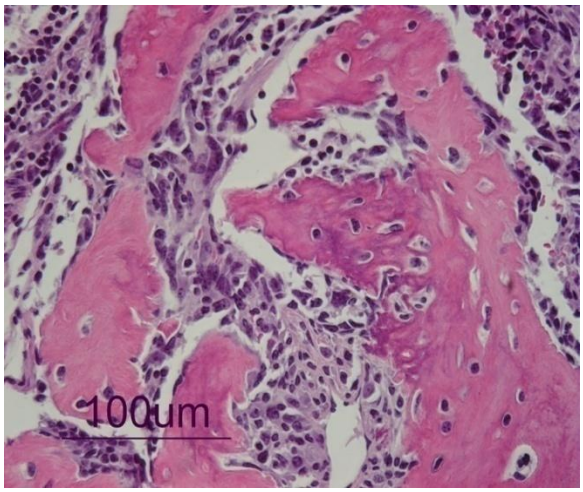

Figure 18. Excised osteogenic tissue assed with hematoxylin and eosin staining. The construct was removed eight weeks after *in vivo* growth. Consultation with a pathologist confirmed the formation of bone formation of the mMSC construct. The red-pink regions are areas of mineralization.

CHAPTER 4: SUMMARY AND SUGGESTED FUTURE WORK

Summary

Mechanical properties of engineered tissues were measured using MRE both *in vitro* and *in vivo* with a 9.4T MR scanner. The process of *in vitro* MRE was demonstrated from cell preparation to the generation of an elastogram. As was shown in Figure 6, the differentiation of mesenchymal stem cells had similar differentiation rates as those presented by McBeath et al. (2004). By applying a nondestructive mechanical assessment method to the tissue engineering pipeline, mechanical changes in engineered constructs were evaluated throughout multiple stages of development.

Although further testing is needed, it is possible to pursue correlations between MR properties and MRE measurements as has been previously indicated (Xu et al., 2006). Similar to the paper by Xu et al., the osteogenic axial images shown in Figure 8 displayed a decrease in signal intensity from week one to week four as well as the MR properties in Figure 9 noted a decrease for T_1, T_2, and apparent diffusion coefficient values over the same period. The assessment of such properties is useful; however, none of the MR property values showed as clear of contrast between the growth stages as the assessment using elastography. The range of assessment for MRE can span five orders of magnitude in contrast to only two orders of magnitude for T_1 relaxation measurement (Mariappan et al., 2010).

Furthermore, in comparison to the desired parameters of natural bone (Young's modulus 0.6-3 GPa, (Cowin, 1989)), the osteogenic constructs by week four as shown in Table 1 attained a shear modulus of 22.11 kPa (Young's modus 66.33 kPa). Although the construct measurement indicates a lower stiffness, the measurement did provide

feedback that the current combination of cells, scaffold, and differentiation factors will not produce a construct that would be a suitable bone replacement. On the other hand, the shear stiffness of the adipogenic constructs after four weeks attained a shear modulus 1.19 kPa (Young's modulus 3.57 kPa). Similarly, clinical MRE assessment of native adipose tissue within the breast determined the Young's modulus to be 0.5 to 25 kPa (van Houten et al., 2003).

As an extension of the TE testing process an original MRE system for *in vivo* testing was developed. Shear waves were observed in both osteogenic and adipogenic constructs; however only the adipogenic constructs produced multiple waves within the tissue. Furthermore, the assessment of animal models with MRE even enabled the analysis of an unanticipated development.

As noted in the literature, mMSCs have the occasional tendency to progress toward the formation of carcinoma (Miura et al., 2006; Tasso et al., 2009). More precisely, the tumors produced from mMSCs developed into cases of pathologist diagnosed osteosarcoma and fibrosarcoma. Although tumors formation is not desirable in tissue development applications, in cancer research tumor formation provides a reliable model for evaluating oncogenesis. One dynamic of this process that will benefit from further study is the noninvasive evaluation of tissue/ tumor stiffness. In alignment with IACUC protocols all mice were euthanized once tumors reached 1.5 cm along the longest axis. However, prior to euthanasia no noticeable changes in mouse behavior were evident between the tumor mice and those in which a tumor did not form. In the differentiation study two mice developed tumors and were assessed noting a change of stiffness that ranged from 9 kPa to 27 kPa at termination of the study.

Tumor formation was noted 6 weeks after implantation. Seven weeks after implantation the first mouse was evaluated using magnetic resonance elastography. Figure 19 shows a traditional magnitude image of the tumor as well as its correlating shear motion image and elastogram. The average stiffness for the tumor was 18.6 kPa and the region with notably higher stiffness measured was 27.4 kPa. T_1 and T_2-weighted images were also acquired as shown in Figure 20. Cross sections of the tumor, as shown in Figure 21, illustrate the morphology of the tumor. Analysis conducted *ex vivo* determined that the tumor's stiffness was 20.4 kPa as displayed in Figure 22.

The ability for MRE to evaluate tumors non-invasively holds promise for assessment in future studies. If assessed in the early stages of tumor development this technique could provide valuable information as to the changes in a tumor's mechanical properties throughout each growth stage for diseases such as breast cancer (McKnight et al., 2002). The tumor assessed in the study was diagnosed by a pathologist as being an osteosarcoma. Although these tumors were produced from the use of immortalized mMSC cells the study produced a model for generating and assessing tumor formation, which until now has been mainly a focus at the clinical scale.

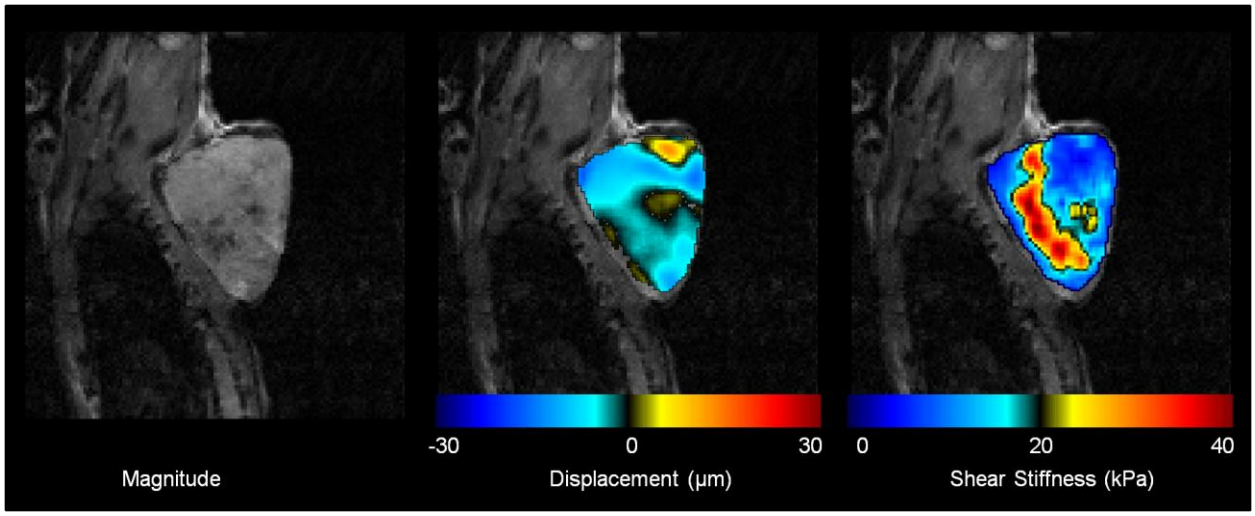

Figure 19. Tumor with shear wave. The parameters used to acquire the shear wave images were as follows: repetition time, 1200 ms; echo time, 27.02 ms; slice thickness, 1 mm; averages, 2; field-of-view,3.0 cm x 3.0 cm; in-plane resolution, 234 μm x 234 μm; actuator frequency, 640 Hz; gradient amplitude, 40 G/cm; bipolar pairs, 4.

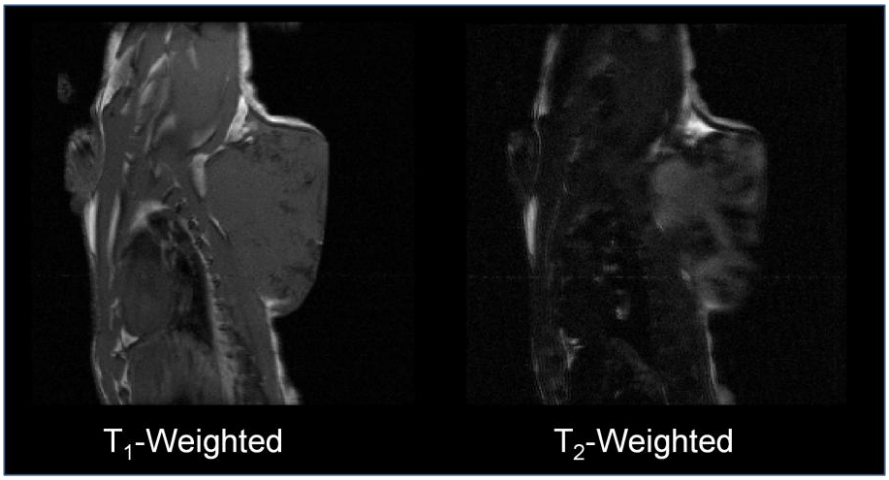

Figure 20. MR weigheted images illustrate variety of tissue types present in the tumor. The T_1-weighted image was acquired using a fast spin-echo sequence with repetition time, 600 ms; echo train length, 4; echo spacing, 8.92 ms; kspace-encodings, 1; field-of-view, 3.0 cm x 3.0 cm; in-plane resolution, 117 μm x 117 μm; slice thickness, 1 mm; averages, 16. The T_2-weighted image was acquired using a fast spin-echo sequence with repetition time, 3000 ms; echo train length, 8; echo spacing, 25 ms; kspace encodings, 4; field-of-view, 3.0 cm x 3.0 cm; in-plane resolution, 117 μm x 117 μm; slice thickness, 1 mm; averages, 16.

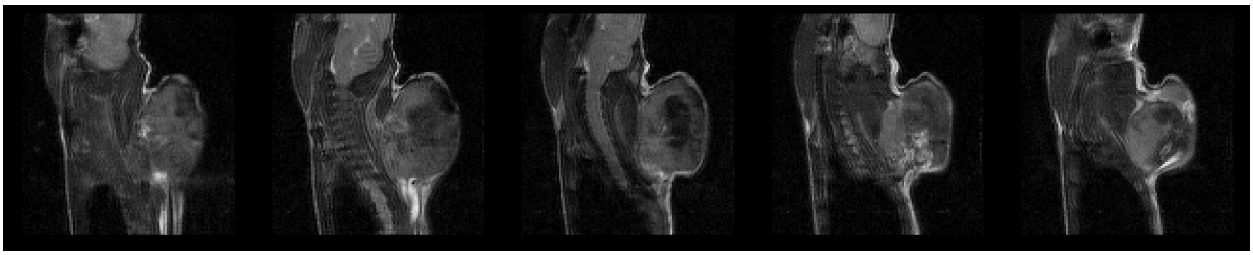

Figure 21. Fast spin-echo image showing cross-sections of the tumor body. Note the bone-like core that formed in the mice. The image parameters were TR, 2000 ms; ETL, 8; ESP, 10 ms; kzero, 4; field-of-view, 3.0 cm x 3.0 cm; in-plane resolution, 234 μm x 234 μm; slice thickness, 1 mm; slices, 5; gap, 0.5 mm; averages, 2.

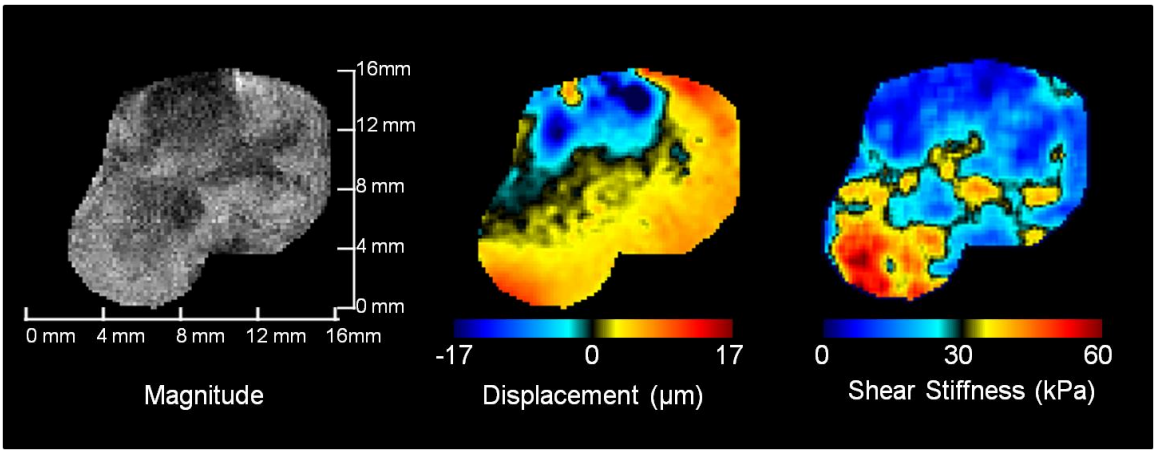

Figure 22. *Ex vivo* assessment of tumor with correlating shear wave and elastogram. The parameters used to acquire the shear wave images were as follows: repetition time, 1000 ms; echo time, 29.2 ms; slice thickness, 1 mm; averages, 1; field-of-view, 2.5 cm x 2.0 cm; in-plane resolution, 195 μm x 156 μm; actuator frequency, 545 Hz; gradient amplitude, 60 G/cm; bipolar pairs, 4.

Suggestions

When performing MRE experiments, a few limitations should be noted. The assessment of *in vitro* specimens is a time sensitive study. Therefore, it is recommended that studies should last no more than one hour so that any potential damage to the tissue construct is minimized. Additionally, faithful recovery of the stiffness map can be compromised due to constructs being either too small or stiff (Oliphant et al., 2001). The size and measured stiffness limitations in MRE, apparent from *in vivo* data, arise from the collected displacement data and noise distribution. The noise distribution in shear wave images can be different and it depends on the two acquisitions. The difference can arise from system instabilities and imperfections, such as eddy currents produced by toggled bipolar gradients, and fluctuation of the RF receiving chain (Othman et al., 2006). The available sample size places a constraint on the maximum measurable shear wavelength, λ_s, since the wavelength depends on the material stiffness and acoustic excitation frequency ($\sqrt{\mu/\rho} = f\lambda_s$) and the shear wave image resolution Δx places a constraint on the minimum wavelength, thus:

$$2\ \mathrm{FOV} \geq \lambda_s \geq 2\Delta x,$$

Where $2\Delta x$ is the minimum wavelength based on the Nyquist criterion with half a wavelength to estimate the shear stiffness as mentioned previously.

The above limitations are important to address as they represent hurdles to reconstructing elastograms. Furthermore, to compute the stiffness, the spatial resolution plays an important role. It has been shown that, for assessing the stiffness of a homogeneous material, at least half a wavelength should be visible. This was the case of the temporal muscle where a stiffness of 15 kPa was calculated as measured from

Figure16, but because of its small size (around 6 mm), the stiffness of the engineered tissue construct could not be evaluated. Considering that the mechanical actuator was driven at 400 Hz and using 1000 kg/m3 for the density, the expected wavelength was around 14 cm. Thus a length of about 7 cm of tissue construct should be available in order to assess a proper value for the stiffness. One possible solution to this problem is to operate at higher frequency (> 2.5 kHz), as the wavelength is inversely proportional to the frequency. Piezoelectric stack actuators driven by high voltage amplifiers are able to deliver sufficient motion at such frequencies to produce a full shear wavelength in the sample. Given the same experiment, in order for half a wavelength to be visible in the 6 mm long construct, a frequency of at least 4600 Hz should have been used. A potential *in vivo* testing design utilizing a stack actuator is shown in Figure 23. It should also be noted that while moving to high frequency will provide a decreased wavelength, the higher frequencies can suffer from problems of attenuation if the supplied displacement is not sufficient (Lopez et al., 2008).

Another possible pursuit for this project could be the incorporation of the MRE sequence into faster sequences such as fast spin-echo and echo planar imaging (Rydberg et al., 2001; Kruse et al., 2006). Through the use of faster sequence there is the potential for either the acquisition of more phase offsets that could provide more robust datasets for calculation of shear stiffness or the assessment of more slices within a single session would help in mapping the stiffness within larger constructs.

As a means of cross verification of the MRE data, the development of either nanoindentation or dynamic mechanical analysis should be pursued. Both devices are capable of conducting frequency specific analysis to give a shear modulus measurement.

Beyond the possibilities *in vitro* and ectopic studies, the next step of pre-clinical assessment is to evaluate the effectiveness of tissue in tissue defects. These studies would potentially provide a better understanding of how to produce longer lasting functional implants for use in regenerative medicine.

Imaging techniques have the potential to greatly advance the field of TE if they provide the tissue engineer with quantitative measurement reflective of the structure, composition, and function of the tissue during the regenerative process. By measuring the mechanical properties and their respective changes over a time course, estimations of functional tissue development can be calculated leading to a better understanding of tissue growth and host tissue integration.

Figure 23. Potential *in **vivo*** piezoelectric stack actuator system**. T**he MRE probe will be capable of high resolution elasticity analysis at frequencies greater than 2.5 kHz.

REFERENCES

Alhadlaq, A., Elisseeff, J. H., Hong, L., Williams, C. G., Caplan, A. I., Sharma, B., Kopher, R. A., Tomkoria, S., Lennon, D. P., Lopez, A., and Mao, J. J. Adult stem cell driven genesis of human-shaped articular condyle. *Annals of Biomedical Engineering*. 2004; 32: 911-923.

Alhadlaq, A. and Mao, J. J. Mesenchymal stem cells: isolation and therapeutics. *Stem Cells and Development.* 2004; 13:436-448.

Altman, G. H., Horan, R. L., Martin, I., Farhadi, J., Stark, P. R. H., Volloch, V., Richmond, J. C., Vunjak-Novakovic, G., and Kaplan, D. L. Cell differentiation by mechanical stress. *The FASEB Journal*. 2001; 16: 70–272.

American Society of Plastic Surgeons. Report of the 2010 plastic surgery statistics [Internet]. American Society of Plastic Surgeons Plastic Surgery Foundation; 2011 [cited 2011 May31]. Available from: http://www.plasticsurgery.org/ Documents/news-resources/statistics/2010-statisticss/Top-Level/2010-US-cosmetic-reconstructive-plastic-surgery-minimally-invasive-statistics2.pdf.

Bernstein, M. A., King, K. F., and Zhou, X. J. *Handbook of pulse sequences*. Elsevier: Burlington, MA; 2004.

Butler, D. L., Goldstein, S. A., and Guilak, F. Functional tissue engineering: the role of biomechanics. *Journal of Biomechanical Engineering*. 2000; 122: 570-575.

Caplan, A. I. The mesengenic process. *Clinics in Plastic Surgery*. 1994; 21: 429-435.

Choi, J. H., Gimble, J. M., Lee, K., Marra, K. G., Rubin, J. P., Yoo, J. J., Vunjak-Novakovic, G., and Kaplan, D. L. Adipose tissue engineering for soft tissue regeneration. *Tissue Engineering: Part B, Reviews*. 2010; 16: 413-26.

Clayton, E. H., Garbow, J. R., and Bayly, P. V. Frequency-dependent viscoelastic parameters of mouse brain tissue estimated by MR elastography. *Physics in Medicine and Biology*. 2011; 56: 2391-2406.

Dado, D. and Levenberg, S. Cell-scaffold mechanical interplay within engineered tissue. *Seminars in Cell and Developmental Biology*. 2009; 20: 656-664.

Derubeis, A. R. and Cancedda, R. Bone marrow stromal cells (BMSCs) in bone engineering: limitations and recent advances. *Annal of Biomedical Engineering.* 2004; 32: 160-165.

Friedenstein, A. J. Precursor cells of mechanocytes. *International Review of Cytology*. 1976; 47: 327-359.

Graff, KF**.** *Wave motion in elastic solids.* New York : Dover, 1999.

Greenwald, A. S., Boden, S. D., Goldberg, V. M., Khan, Y., Laurencin, C. T., and Rosier, R. N. Bone-graft substitutes: facts, fictions, and applications. *The Journal of Bone and Joint Surgery.* 2001; 83-A Suppl 2 Pt 2:98-103.

Glowacki, J. and Mizuno, S., Collagen scaffolds for tissue engineering. *Biopolymers.* 2008; 89: 338-344.

Haacke, E. M., Brown, R. B., Thompson, M. R., and Venkateson, R. *Magnetic resonance imaging: physical principals and sequence design*. John Wiley & Sons: New York, 1999.

Hartman, E. H., Pikkemaat, J. A., Vehof, J. W., Heerschap, A., Jansen, J. A., and Spauwen, P. H. *In vivo* magnetic resonance imaging explorative study of ectopic bone formation in the rat. *Tissue Engineering*. 2002; 8: 1029-1036.

Helmchen, F. and Denk, W. Deep tissue two-photon microscopy. *Nature Methods.*2005; 2: 932-940.

Heng, B. C., Cao T., Stanton, L.W., Robson, P., and Olsen, B. Strategies for directing the differentiation of stem cells into the osteogenic lineage *in vitro*. *Journal of Bone Mineral Research*. 2004; 19: 1379-1394.

Hong, L., Peptan, I. A., Clark, P., and Mao, J.J. Ex-vivo adipose tissue engineering by human marrow stromal cell seeded gelatin sponge. *Annals of Biomedical Engineering.* 2005; 33: 511–517.

Ishihara Y, Calderon A, Watanabe H, Okamoto K, Suzuki Y, Kuroda K, Suzuki Y. A precise and fast temperature mapping using water proton chemical shift. *Magnetic Resonance in Medicine*. 1995; 34: 814-823.

Jones, J. R., Atwood, R. C., Poologasundarampillai, G., Yue, S., and Lee, P. D. Quantifying the 3D macrostructure of tissue scaffolds. *Journal of Materials Science: Materials in Medicine.*2009; 20: 463-471.

Kotlarchyk, M. A., Botvinick, E. L., and Putnam A. J. Characterization of hydrogel microstructure using laser tweezers particle tracking and confocal reflection imaging. *Journal of Physics: Condensed Matter.* 2010; 22: 194121.

Kim, K., Jeong, C. G., and Hollister, S. J. Non-invasive monitoring of tissue scaffold degradation using ultrasound elasticity imaging. *Acta Biomaterialia.* 2008; 4: 783-790.

Kruse, S.A., Grim, R.C., Lake, D.S., Manduca, A. & Ehman, R.L. Fast EPI based 3D MR elastography of the brain. In Proceedings of the International Society for Magnetic Resonance in Medicine. 2006. Seattle, Washington. p 3385.

Langer, R. and Vacanti, J. P. Tissue engineering. *Science.* 1993*;* 260: 920-926.

Leong, K. F., Cheah, C. M., and Chua, C. K. Solid freeform fabrication of three-dimensional scaffolds for engineering replacement tissues and organs. *Biomaterials*. 2003; 24: 2363-2378.

Lopez, O., Amrami, K. K., Manduca, A., and Ehman, R. L. Characterization of the dynamic shear properties of hyaline cartilage using high-frequency dynamic MR elastography. *Magnetic Resonance in Medicine.* 2008; 59: 356-364.

Magli, M. C., Levantini, E., and Giogetti, A. Developmental potential of somatic stem cells in mammalian adults. *Journal of Hematotherapy and Stem Cell Research.* 2000; 9: 961-969.

Manduca, A., Oliphant, T. E., Dresner, M. A., Mahowald, J. L., Kruse, S. A., Amromin, E., Felmlee, J. P., Greenleaf, J. F., and Ehman R. L. Magnetic resonance elastography: non-invasive mapping of tissue elasticity *Medical Image Analysis* 2001; 5: 237-254.

Marion, N. W. and Mao, J. J. Mesenchymal stem cells and tissue engineering. *Methods in Enzymology*. 2006; 420: 339-361.

Mauck, R. L, Soltz, M. A., Wang, C. C., Wong, D. D., Chao, P. H., Valhmu, W. B., Hung, C. T., and Ateshian, G. A. Functional tissue engineering of articular cartilage through dynamic loading of chondrocyte-seeded agarose gels. *Journal of Biomechanical Engineering*. 2000; 122: 252-260.

Mariappan, Y. K., Glaser, K. J., and Ehman R. L. Magnetic resonance elastography: a review. *Clinical Anatomy*. 2010; 23:497-511.

McBeath, R., Pirone, D. M., Nelson, C. M., Bhadriraju, K., and Chen, C. S. Cell shape, cytoskeletal tension, and RhoA regulate stem cell lineage commitment. *Developmental Cell*. 2004; 6: 483-495.

McKnight, A. L., Kugel, J. L., Rossman, P. J., Manduca, A., Hartmann, L. C., Ehman, R. L. MR elastography of breast cancer: preliminary results. *American Journal of Roentgenology*. 2002; 178: 1411-1417.

Mistry, A. S. and Mikos, A. G. Tissue engineering strategies for bone regeneration. *Advances in Biochemical Engineering/ Biotechnology*. 2005; 94:1-22.

Miura, M., Miura, Y., Padilla-Nash, H. M., Molinolo, A. A., Fu, B., Patel, V., Seo, B. M., Sonoyama, W., Zheng, J. J., Baker, C. C., Chen, W., Ried, T., and Shi S. Accumulated chromosomal instability in murine bone marrow mesenchymal stem cells leads to malignant transformation. *Stem Cells.*2006; 24: 1095–1103.

Moran, P. R., Moran, R. A., and Karstaedt, N. Verification and evaluation of internal flow and motion. True MRI by the phase gradient modulation method. *Radiology* 1985; 154: 433-441.

Muthupillai, R., Lomas, D. J., Rossman, P. J., Greenleaf, J.F., Manduca, A., and Ehman, R. L. Magnetic resonance elastography by direct visualization of propagating acoustic strain waves. *Science*. 1995; 29:1854-1857.

Muthupillai, R., Rossman, P. J., Lomas, D. J., Greenleaf, J. F., Riederer, S. J., and Ehman, R. L. Magnetic resonance imaging of transverse acoustic strain waves. *Magnetic Resonance in Medicine*. 1996; 36:266-274.

Oliphant, T. E., Manduca, A., Ehman, R. L., and Greenleaf, J. F. Complex-valued stiffness reconstruction for magnetic resonance elastography by algebraic

inversion of the differential equation.*Magnetic Resonance in Medicine.* 2001; 45: 299-310.

Othman, S. F., Xu, H., Royston, T. J., and Magin, R. L. Microscopic magnetic resonance elastography. *Magnetic Resonance in Medicine*. 2005; 54: 605-615.

Othman, S. F., Curtis, E. T., Plautz, S. A., Pannier, A. P. & Xu, H. Magnetic resonance elastography monitoring of tissue engineered constructs. *NMR in Biomedicine*. 2011; 24: n/a.

Othman, S. F., Zhou, X. J., Xu, H., Royston, T. J., and Magin, R. L. Error propagation model for microscopic magnetic resonance elastography shear-wave images. *Magnetic Resonance in Medicine*. 2006; 25(1): 94-100.

Patrick, C. W. Tissue engineering strategies for adipose tissue repair. *The Anatomical Record*. 2001; 263; 361-366.

Patrick, C. W., Uthamanthil, R., Beahm, E., and Frye, C. Animal models for adipose tissue engineering. *Tissue Engineering: Part B, Reviews.*2008; 14: 167-178.

Peptan, I. A., Hong, L., Xu, H., and Magin, R. L. MR assessment of osteogenic differentiation in tissue-engineered constructs. *Tissue Engineering*. 2006; 12: 843-851.

Pittenger, M. F., Mackay, A. M., Beck, S. C., Jaiswal, R. K., Douglas, R., Mosca, J., D., Moorman, M. A., Simonetti, D. W., Craig, S., and Marshak, D. R. Multilineage potential of adult human mesenchymal stem cells. *Science.* 1999. 284: 143-147.

Potter, K., Sweet, D. E., Anderson, P., Davis, G. R., Isogai, N., Asamura, S., Kusuhara, H., and Landis, W. J. Non-destructive studies of tissue-engineered phalanges by

magnetic resonance microscopy and X-ray microtomography. *Bone.* 2006; 38: 350-358.

Ringleb, S. I., Chen, Q., Lake, D. S., Manduca, A., Ehman R.L., and An, K. Quantitative shear wave: comparison to a dynamic shear material test. *Magnetic Resonance in Medicine* 2005; 53: 1197-1201.

Rydberg, J., Grimm, R., Kruse, S., Felmlee, J., McCracken, P. and Ehman, R.L. Fast spin-echo magnetic resonance elastography of the brain. In: Proceedings of the International Society of Magnetic Resonance in Medicine. 2001. Glasgow, Scotland. p 1647.

Rozen, W. M., Rajkomar, A. K., Anavekar, N. S., and Ashton, M. W., Post-mastectomy breast reconstruction: a history in evolution. *Clinical Breast Cancer*. 2009; 9: 145-154.

Sabokbar, A., Millett, P. J., Myer, B., and Rushton N. A rapid, quantitative assay for measuring alkaline phosphatase activity in osteoblastic cells *in vitro*. *Bone and Mineral*. 1994; 27: 57-67.

Tasso, R., Augello, A., Carida', M., Postiglione, F., Tibiletti, M.G., Bernasconi, B., Astigiano, S., Fais, F., Truini, M., Cancedda, R., and Pennesi, G. Development of sarcomas in mice implanted with mesenchymal stem cells seeded onto bioscaffolds. *Carcinogenesis*. 2009; 30: 150-157.

Tsang, V. L. and Bhatia, S. N. Three-dimensional tissue fabrication. *Advanced Drug Delivery Reviews*. 2004; 56: 1635-1647.

Van Houten, E. E., Doyley, M. M., Kennedy, F. E., Weaver, J. B., and Paulsen, K. D. Initial in vivo experience with steady-state subzone-based MR elastography of the human breast. *Journal of Magnetic Resonance Imaging*. 2003; 17:72-85.

Washburn, N.R., Weir, M., Anderson, P., and Potter, K. Bone formation in polymeric scaffolds evaluated by proton magnetic resonance microscopy and X-ray microtomography. *Journal of Biomedical Research: Part A.* 2004: 69: 738-747.

Wuerfel, J., Paul, F., Beierbach, B., Hamhaber, U., Klatt, D., Papazoglou, S., Zipp, F., Martus, P., Braun, J., and Sack I. MR-elastography reveals degradation of tissue integrity in multiple sclerosis. *NeuroImage.* 2010; 49: 2520-2525.

Xu, H., Othman S. F., and Magin, R. L. Monitoring tissue engineering using magnetic resonance imaging. *Journal of Bioscience and Bioengineering*. 2008; 106: 515-527.

Xu, H., Othman, S. F., Hong, Peptan, I. A., Magin, R. L. Magnetic resonance microscopy for monitoring osteogenesis in tissue-engineered construct *in vitro*. *Physics in Medicine and Biology*. 2006; 51: 719-732.

Yaszemski, M. J., Payne, R. G., Hayes, W. C., Langer, R., and Mikos, A. G. Evolution of bone transplantation: molecular, cellular and tissue strategies to engineer human bone. *Biomaterials*. 1996; 17: 175-185.

APPENDIX A: *IN VIVO* ACTUATOR DESIGNS

The initial design for the animal actuator is show in Figure 24. Although the design offered diversity in the amount of places and orientation that the actuator could be placed, the sheer number of screws and adjustment points made this approach difficult to assemble in a short period of time. Also note that of the 12 adjustable 2-56 nylon screws, there are points of rotation at which turning these screws was not possible.

The next design that was developed was a simplified version that made use of the archway above the animal positioning holder. Notches were placed in 0.125" (3.175 mm) intervals along the 0.25" (6.35 mm) rod. This method increased accessibility; however, coupling between the surface of the mouse and the actuator was often an issue that resulted in no wave propagation.

A redesign rotated the actuator beam 90° and change the motion from one of sweeping across the back of the animal to one more closely resembling a hammer motion. This method provided more consistent wave results; however, the current contact point sank a couple of millimeters into the back of the mouse creating undue tension on the skin of the mouse.

The current method makes use of the same principal of applying motion normal to the back of the mouse. However, by increasing the contact area between the actuator and the mouse the system was able to maintain adequate coupling without deforming the region around the construct.

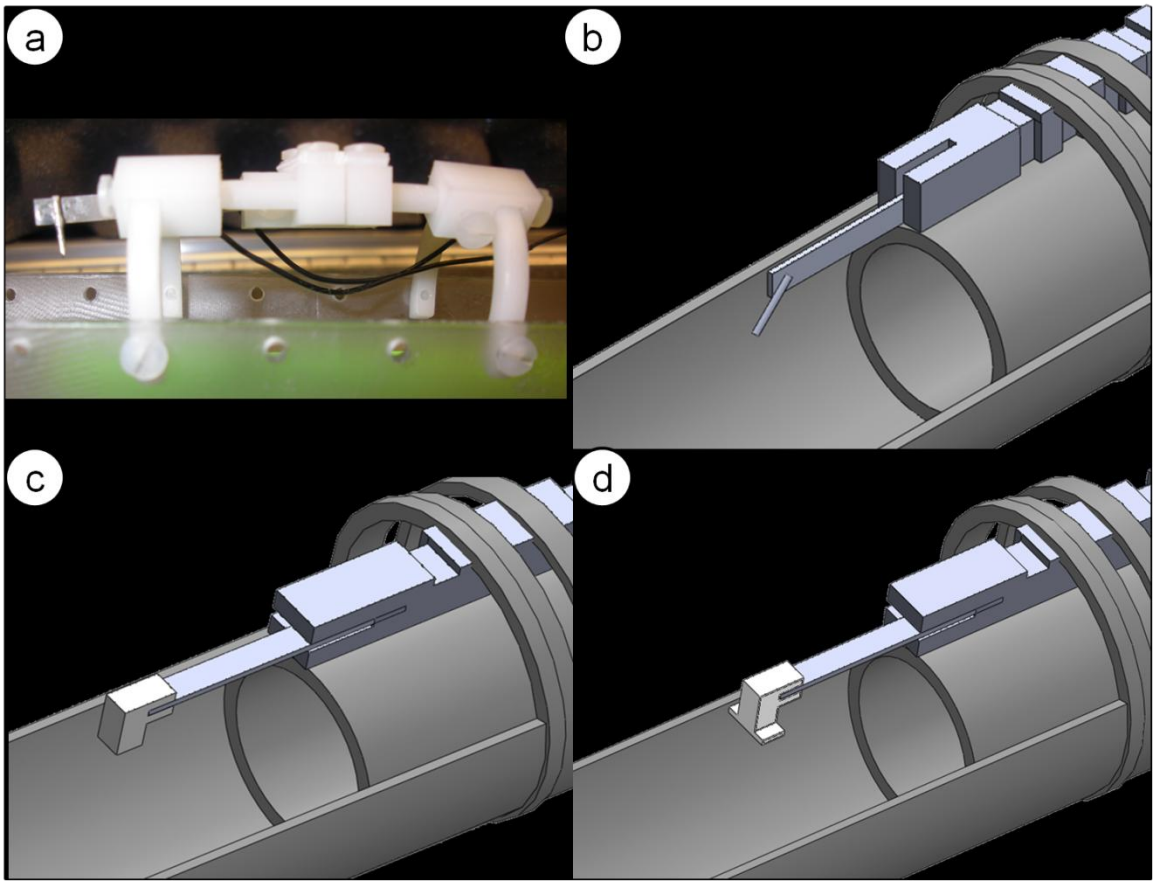

Figure 24. *In vivo* actuator designs. (a) A highly adjustable design was originally implemented with the intention of providing the operator complete control over the placement of the actuator. (b) The system was reduced to needing only two nylon screw and no longer was attached over the body of the animal. (c) The actuator was rotated 90° and the tip was replaced with an elbow design. (d) Contact area between the actuator and the back of the mouse was increased.